JACS
JOURNAL OF THE AMERICAN CHEMICAL SOCIETY
pubs.acs.org/JACS

Article

Proton-Detected Solid-State NMR for Deciphering Structural Polymorphism and Dynamic Heterogeneity of Cellular Carbohydrates in Pathogenic Fungi

Jayasubba Reddy Yarava,*,‡ Isha Gautam,‡ Anand Jacob, Riqiang Fu, and Tuo Wang*

Cite This: J. Am. Chem. Soc. 2025, 147, 17416–17432

Read Online

ACCESS | Metrics & More | Article Recommendations | Supporting Information

ABSTRACT: Carbohydrate polymers in their cellular context display highly polymorphic structures and dynamics essential to their diverse functions, yet they are challenging to analyze biochemically. Proton-detection solid-state NMR spectroscopy offers high isotopic abundance and sensitivity, enabling the rapid and high-resolution structural characterization of biomolecules. Here, an array of 2D/3D ^{1}H-detection solid-state NMR techniques are tailored to investigate polysaccharides in fully protonated or partially deuterated cells of three prevalent pathogenic fungi: *Rhizopus delemar*, *Aspergillus fumigatus*, and *Candida albicans*, representing filamentous species and yeast forms. Selective detection of acetylated carbohydrates reveals 15 forms of *N*-acetylglucosamine units in *R. delemar* chitin, which coexists with chitosan, and associates with proteins only at limited sites. This is supported by distinct order parameters and effective correlation times of their motions, analyzed through relaxation measurements and model-free analysis. Five forms of α-1,3-glucan with distinct structural origins and dynamics were identified in *A. fumigatus*, important for this buffering polysaccharide to perform diverse roles of supporting wall mechanics and regenerating a soft matrix under antifungal stress. Eight α-1,2-mannan side chain variants in *C. albicans* were resolved, highlighting the crucial role of mannan side chains in maintaining interactions with other cell wall polymers to preserve structural integrity. These methodologies provide novel insights into the functional structures of key fungal polysaccharides and create new opportunities for exploring carbohydrate biosynthesis and modifications across diverse organisms.

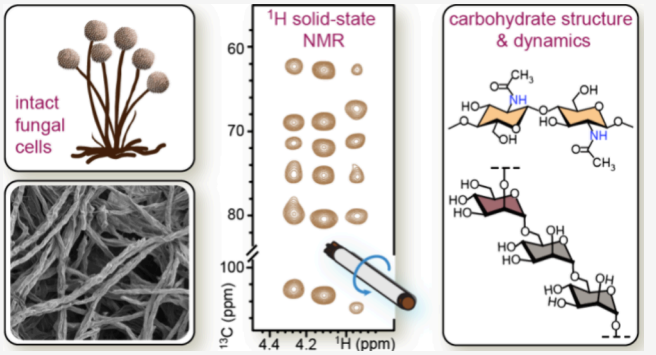

INTRODUCTION

Carbohydrate and glycoconjugates, such as polysaccharides, glycoproteins, proteoglycans, and glycolipids, play critical roles in immunobiological processes and cellular communication, act as energy and carbon reservoirs, and provide structural support to cells across various organisms.[1−4] The carbohydrate-rich cell walls of plants, fungi, and bacteria are crucial for maintaining cell shape and integrity while also regulating mechanical properties, adhesion, and extensibility.[4,5] In addition, the structure and biosynthesis of microbial carbohydrates serve as key targets for the development of antibiotics and antifungal therapies aimed at addressing the rising challenge of antibiotic and antifungal resistance.[6−9] The biological functions of carbohydrates are largely dictated by their structure and properties; however, these molecules are typically highly complex in their native cellular state.[10,11] This complexity arises from several factors, including diverse covalent linkages between monosaccharide units and their linkage to other molecules, such as proteins and lipids, highly variable monosaccharide compositions, broad conformational distributions, higher-order supramolecular assemblies, interactions with neighboring molecules, and extensive chemical modifications, such as acetylation and methylation.[12,13] Such complexity has presented challenges for high-resolution characterization of cellular polysaccharides.[13]

In recent years, solid-state NMR spectroscopy has emerged as a powerful tool for correlating the structure and function of polysaccharides in intact cells and tissues without requiring dissolution or extraction, and when integrated with structural insights from biochemical and imaging techniques, it provides a comprehensive understanding of polysaccharide organization and interactions.[14−16] Applications to bacterial samples have enabled the quantification of molecular composition, provided insights into cell wall architecture and antibiotic responses, and identified structural factors influencing cell adherence and biofilm formation.[17−21] In plants, solid-state NMR has unveiled the overlooked role of pectin in interacting with cellulose, as well as the impact of pectin methylation and calcium chelation in

Received: March 7, 2025
Revised: April 20, 2025
Accepted: April 23, 2025
Published: May 6, 2025

primary plant cell walls.[22−24] It has also revealed the diverse helical screw conformations of xylan that facilitate its interactions with cellulose and lignin in secondary plant cell walls.[25−29] In fungal species, solid-state NMR has been instrumental in defining the structural roles of key polysaccharides—including chitin, glucans, chitosan, mannan, and galactan-based polymers—in cell wall organization, capsule structure, and the melaninization process.[30−35] Most of these studies utilize ^{13}C and ^{15}N to resolve the vast number of distinct sites in carbohydrates and proteins within the cellular samples, but ^{1}H offers higher sensitivity, faster acquisition, and reduced sample requirements due to its greater gyromagnetic ratio and natural isotopic abundance. Meanwhile, advancements in ^{1}H-based solid-state NMR for protein structural biology inspire efforts to adapt these methods for systematic investigations of carbohydrate polymers with diverse structures.[36−39]

Direct detection of protons in biomolecular solid-state NMR was first introduced for peptides and proteins through the perdeuteration approach, which enhances spectral resolution by replacing protons with deuterium at nonexchangeable sites while allowing partial reprotonation at exchangeable sites, thereby significantly reducing proton density.[40,41] Subsequent advancements, including isotopic dilution, fast magic-angle spinning (MAS), high-field magnets, and triple-resonance experiments, facilitated the determination of protein three-dimensional structures.[36−38,40−47] Improvements in probe technology have enabled increasingly rapid sample spinning, with Samoson and colleagues recently achieving 160−170 kHz MAS.[48−50] The commercial availability of ultrahigh magnetic fields, such as 1.2 GHz (28 T),[42] along with advanced sample preparation protocols,[51−55] has greatly expanded the applicability of ultrafast MAS techniques to diverse biological systems, including globular microcrystalline proteins;[48,56] disordered proteins;[57] membrane proteins;[58] nucleic acids;[59] viruses, e.g., HIV[60] and SARS-CoV-2;[61] biofilms;[62] and amyloids.[63,64] Fast-MAS techniques have also been widely applied to unlabeled small molecules, including pharmaceutical drugs, facilitating the identification of hetero- and homosynthons, characterization of crystal forms (e.g., salt cocrystals and continuum forms), and elucidation of hydrogen-bonding networks and three-dimensional crystal packing arrangements.[65−70]

^{1}H-detection and ultrafast MAS were also used to determine protein dynamics. The spin relaxation process provides valuable information about local protein motions, but in solids, unaveraged coherences significantly influence relaxation, complicating the quantification of dynamics. These unaveraged coherences are largely eliminated by applying ultrafast MAS rates in combination with sample perdeuteration, which, along with advanced spin relaxation models, enable quantitative analysis of protein motions across a wide range of time scales, including fast motions (ps-ns), slow motions (ns-μs), and slow conformational dynamics (μs-ms).[71−73] These methods were initially applied to small globular proteins using the simple model-free (SMF) approach, revealing order parameters and effective correlation times, while the extended model-free (EMF) approach enabled the observation of motions at two independent time scales, including fast and slow motions, and relaxation dispersion methods were used to investigate slow conformational dynamics.[71,74−78] The development of the Gaussian axial fluctuation (GAF) model revealed anisotropic collective protein motion, and its incorporation into the SMF approach enabled the analysis of both local and global motions in membrane proteins.[79−81] When integrated into the EMF model, GAF allowed the observation of both collective slow motions and fast local motions in membrane proteins.[82] Subsequently, a "dynamics detector method" was implemented to visualize dynamics across a wide range of time scales,[83,84] while ultrafast MAS enabled the direct determination of order parameters through heteronuclear dipolar recoupling.[85−87] Altogether, fast MAS and relaxation models enable the quantitative measurement of the protein dynamics.

Despite these advancements, the application of proton detection methods to the characterization of carbohydrate polymers, particularly in intact cells, remains relatively limited. Hong and colleagues utilized proton-detection experiments under moderately fast MAS to investigate the structure and dynamics of mobile pectin and semimobile hemicellulose, as well as their interactions with cellulose in primary plant cell walls.[88,89] Baldus and colleagues developed scalar- and dipolar-coupling-based techniques to examine the structural organization of carbohydrates in the cell walls of a mushroom-forming fungus *Schizophyllum commune*.[31,34,90] Schanda and colleagues have employed ultrafast MAS to study bacterial peptidoglycan and, more recently, capsule polysaccharides in the yeast cells of *Cryptococcus neoformans*.[33,91,92] We have utilized proton detection to analyze mobile and rigid polysaccharides in several fungal pathogens, observing the unique capability of ^{1}H detection in sensing and resolving local structural variations of carbohydrates within a cellular context.[93−95]

In this study, we adapt a suite of proton-detected solid-state NMR techniques, originally developed for protein structural determination, to investigate the structural polymorphism of polysaccharides in fully protonated and partially deuterated cells of three pathogenic fungal species that cause life-threatening infections in over 600,000 patients worldwide each year, with high mortality even after treatment.[96] The species studied include the filamentous fungi *R. delemar* and *A. fumigatus*, major causes of severe infections like mucormycosis and invasive aspergillosis, as well as the yeast cells of *C. albicans*, the leading cause of candidemia, the fourth most common bloodstream infection in hospitalized patients.[97,98] These fungal species are also the top three contributors to fungal coinfections in COVID-19 patients.[99] The high resolution of ^{1}H, combined with ^{13}C and ^{15}N, provides unprecedented insight into the structural variations of key fungal polysaccharides, including chitin, chitosan, mannan, α-glucan, and β-glucan, thereby laying the foundation for further exploration of the structural and biochemical origins of their structural polymorphism and functional significance in the cellular environment.

A range of 2D and 3D correlation experiments, utilizing engineered polarization transfer pathways through scalar and dipolar couplings, enable the selective filtering of resonances from acetylated amino sugars and their deacetylated forms. These sugars, which are key structural components in fungal chitin, bacterial peptidoglycan, mammalian sialic acids, and glycoproteins, can now be distinguished from the extensive background of other carbohydrates, proteins, and lipids present within the same cells.[100−102] Optimized experimental approaches, including a protocol for adapting microbial growth to a gradually increasing deuteration gradient to improve ^{1}H resolution, have been established for mapping covalently bonded carbon networks in both rigid and mobile phases. Since the cell walls in microorganisms and plants are typically understood as heterogeneous composites, with mechanical domains incorporated into a softer matrix through physical interactions and covalent linkages, this capability allows for the

https://doi.org/10.1021/jacs.5c04054
J. Am. Chem. Soc. 2025, 147, 17416−17432

delineation of carbohydrate contributions and their polymorphic structures within these dynamically distinct regions. Furthermore, relaxation measurements of ^{13}C R_1 and ^{13}C $R_{1\rho}$, analyzed using a simple model-free formalism, allow for the quantification of order parameters and effective correlation times of motions occurring on the picosecond to nanosecond time scale. Although demonstrated on fungal polysaccharides, the proton-detected approaches are applicable to all cellular carbohydrates and glycoconjugates, enabling rapid, high-resolution, and nondestructive analysis of carbohydrate structure and dynamics across diverse living organisms and carbohydrate-based biomaterials.[103−106]

EXPERIMENTAL SECTION

Preparation ^{13}C,^{15}N-Labeled and Deuterated Cells of Four Fungal Species. In this study, intact cells from four fungal species, including the mycelia materials of two filamentous fungi, *Aspergillus fumigatus* and *Rhizopus delemar*, and the yeast cells of *Candida albicans*, were prepared for ^{1}H-detected solid-state NMR experiments. Two *A. fumigatus* samples were prepared in both protonated and deuterated forms, while all other samples are fully protonated. All fungal cells were uniformly ^{13}C, ^{15}N-labeled using growth media enriched with ^{13}C-glucose and ^{15}N-ammonium sulfate or ^{15}N-sodium nitrate (Cambridge Isotope Laboratories). For NMR analysis, approximately 5 mg of each sample was packed into a 1.3 mm magic-angle spinning (MAS) rotor (Cortecnet) for measurements on a 600 MHz spectrometer at the MSU Max T. Roger NMR facility and an 800 MHz NMR at the National High Magnetic Field Laboratory (Tallahassee, FL), while approximately 7 mg of the material was loaded into a 1.6 mm rotor (Phoenix NMR) for measurements on an 800 MHz spectrometer at the MSU Max T. Roger NMR facility. All samples were stored at −20 °C when not being measured, and spectral reproducibility was routinely assessed using 1D and 2D spectra (Figure S1). A fresh batch of samples was prepared whenever changes were observed, and previous studies have demonstrated that fungal cultures prepared using the same protocol exhibit high spectral reproducibility.[94,107−109] The cultivation protocols for each fungal species are described below.

A batch of *A. fumigatus* culture (strain RL 578) was grown in a protonated liquid medium containing ^{13}C-glucose (10.0 g/L) and ^{15}N-sodium nitrate (6.0 g/L), adjusted to pH 6.5. To support optimal fungal growth, the medium was supplemented with 1 mL/L of a mineral-rich trace element solution.[107,109] The stock solution contained the following compounds at the indicated concentrations: $CoCl_2{\cdot}6H_2O$ (1.6 g/L), $CuSO_4{\cdot}5H_2O$ (1.6 g/L), $MnCl_2{\cdot}4H_2O$ (5 g/L), $(NH_4)_6Mo_7O_{24}{\cdot}4H_2O$ (1.1 g/L), $Na_2EDTA{\cdot}4H_2O$ (1.1 g/L), $ZnSO_4{\cdot}7H_2O$ (22 g/L), H_3BO_3 (11 g/L), and $FeSO_4{\cdot}7H_2O$ (5 g/L). The culture was grown for 7 days in 100 mL liquid cultures within 250 mL Erlenmeyer flasks and shaken at 210 rpm at 30 °C. Mycelia were harvested by centrifugation (5000 rpm, 10 min) and subjected to four sequential washes with 10 mM PBS (pH 6.5).

Ten sequential cultures of *A. fumigatus* were prepared under increasing deuterium conditions, with D_2O concentrations ranging from 10 to 100% (v/v), increasing in 10% increments. Each culture step maintained conditions identical to those of the standard protonated medium, except that nanopure water was replaced with the corresponding D_2O/H_2O mixture. To initiate adaptation, 200 μL of *A. fumigatus* grown in a protonated medium was inoculated into 10 mL of a medium containing 10% D_2O in a 50 mL Erlenmeyer flask. Unlabeled glucose and sodium nitrate were used for all intermediate adaptation steps (10−90% D_2O) to reduce costs. After 3 weeks of incubation at 10−40% D_2O, cultures were serially transferred to higher D_2O levels at reduced incubation durations: 2 weeks each at 50−70% D_2O, 10 days each at 80−90% D_2O, and 7 days for the final 100% D_2O step. At each step, 200 μL of culture was transferred into fresh 10 mL of the medium of the next D_2O concentration. For the final culture in 100% D_2O, the culture volume was increased to 50 mL, and the culture was maintained in a 125 mL Erlenmeyer flask. To prepare the sample for NMR analysis, this final culture was supplemented with uniformly labeled ^{13}C-glucose (10.0 g/L) and ^{15}N-sodium nitrate (6.0 g/L). The material was then harvested using centrifugation following the same protocol applied for the protonated culture as described above.

R. delemar (strain FGSC-9543) was initially cultivated on potato dextrose agar (PDA; 15 g/L) at 33 °C for 2 days following inoculation with a scalpel-cut spore fragment placed at the center of the plate.[94] No trace element was used in this medium. Subsequently, the fungus was transferred to a liquid medium containing Yeast Nitrogen Base (YNB; 1.7 g/L, without amino acids and ammonium sulfate; catalog DF0335159 of Thermo Fisher Scientific), ^{13}C-glucose (10.0 g/L), and ^{15}N-ammonium sulfate (6.0 g/L). The culture was maintained at 30 °C for 7 days with the pH adjusted to 7.0. Following growth, cells were harvested by centrifugation (7000 rpm, 20 min) and washed with 10 mM phosphate-buffered saline (PBS, pH 7.4; Thermo Fisher Scientific) to remove small molecules and excess ions.

C. albicans (strain JKC2830) was cultivated in a liquid YNB-based medium (0.67% YNB without amino acids and ammonium sulfate, 10.0 g/L or 2% ^{13}C-glucose, and 5 g/L ^{15}N-ammonium sulfate) in 50 mL Erlenmeyer flasks.[95] No trace element was added to this medium. Cultures were incubated at 30 °C with shaking (20 rpm, Corning LSE) for 24 h. The cells were collected by centrifugation at 1500 rpm for 15 min, and the supernatant was discarded.

Solid-State NMR Experiments. Solid-state NMR experiments were conducted using three high-field NMR spectrometers, including a Bruker Avance Neo 800 MHz (18.8 T) spectrometer at the National High Magnetic Field Laboratory (Tallahassee, FL) equipped with a custom-built 1.3 mm triple-resonance magic angle spinning (MAS) probe, a Bruker Avance-NEO 600 MHz (14.1 T) spectrometer at Michigan State University fitted with a Bruker 1.3 mm triple-resonance HCN probe, and a Bruker Avance-NEO 800 MHz (18.8 T) spectrometer, also at Michigan State University, with a Phoenix 1.6 mm triple-resonance HXY probe and a Bruker 3.2 mm HCN probe.

Sodium trimethylsilylpropanesulfonate (DSS) was added to all samples for calibration of the temperature and referencing of ^{1}H chemical shifts. The ^{13}C chemical shifts were externally calibrated relative to the tetramethylsilane (TMS) scale using the adamantane methylene resonance at 38.48 ppm as the reference. The methionine amide resonance at 127.88 ppm in the model tripeptide N-formyl-Met-Leu-Phe-OH was used for the ^{15}N chemical shift calibration.

A variety of ^{1}H-detected NMR experiments were performed to assign resonances, characterize structural polymorphisms, and investigate the intermolecular packing of cell wall polysaccharides, with pulse sequences illustrated in Figure S2 and phase cycling details provided in Text S1. Experimental conditions varied depending on the fungal and plant species studied, with detailed parameters provided in Tables S1−S4, where *R. delemar* is described in Table S1, deuterated *A. fumigatus* in Tables S2 and S3, and *C. albicans* in Table S4. For all experiments conducted on the 600 MHz spectrometer with a 1.3 mm probe, the MAS rate was set to 60 kHz, with a cooling gas temperature of 250 K, resulting in a sample temperature of 300 K. Some samples were also measured on two 800 MHz NMR spectrometers using different probes, MAS frequencies, and temperature conditions, including *R. delemar* analyzed with a 1.3 mm probe at 60 kHz MAS under 250 K cooling gas and 302 K sample temperature, *R. delemar* and deuterated *A. fumigatus* analyzed using a 1.6 mm probe at 15 kHz and 40 kHz MAS, and mobile molecular components of *C. albicans* examined with a 3.2 mm probe at 15 kHz MAS under 280 K cooling gas and 296 K sample temperature.

At the National High Magnetic Field Laboratory, the temperature of the sample measured using the 1.3 mm MAS probe was calibrated using $Pb(NO_3)_2$ and KBr as a function of MAS frequency. At a MAS frequency of 60 kHz, with the cooling gas temperature set to 250 K, the calibrated temperature was approximately 302 K, which is in general consistent with the temperature (305 K) reported in the literature under identical condition.[36] At MSU, the sample temperature was estimated by measuring the water proton chemical shift relative to the DSS signal at 0 ppm in each sample. We recognize that the cellular pH may cause slight perturbations in the water proton chemical shift, potentially affecting the temperature estimation. Nevertheless, the estimated sample temperatures were generally within the range of 300−

https://doi.org/10.1021/jacs.5c04054
J. Am. Chem. Soc. 2025, 147, 17416−17432

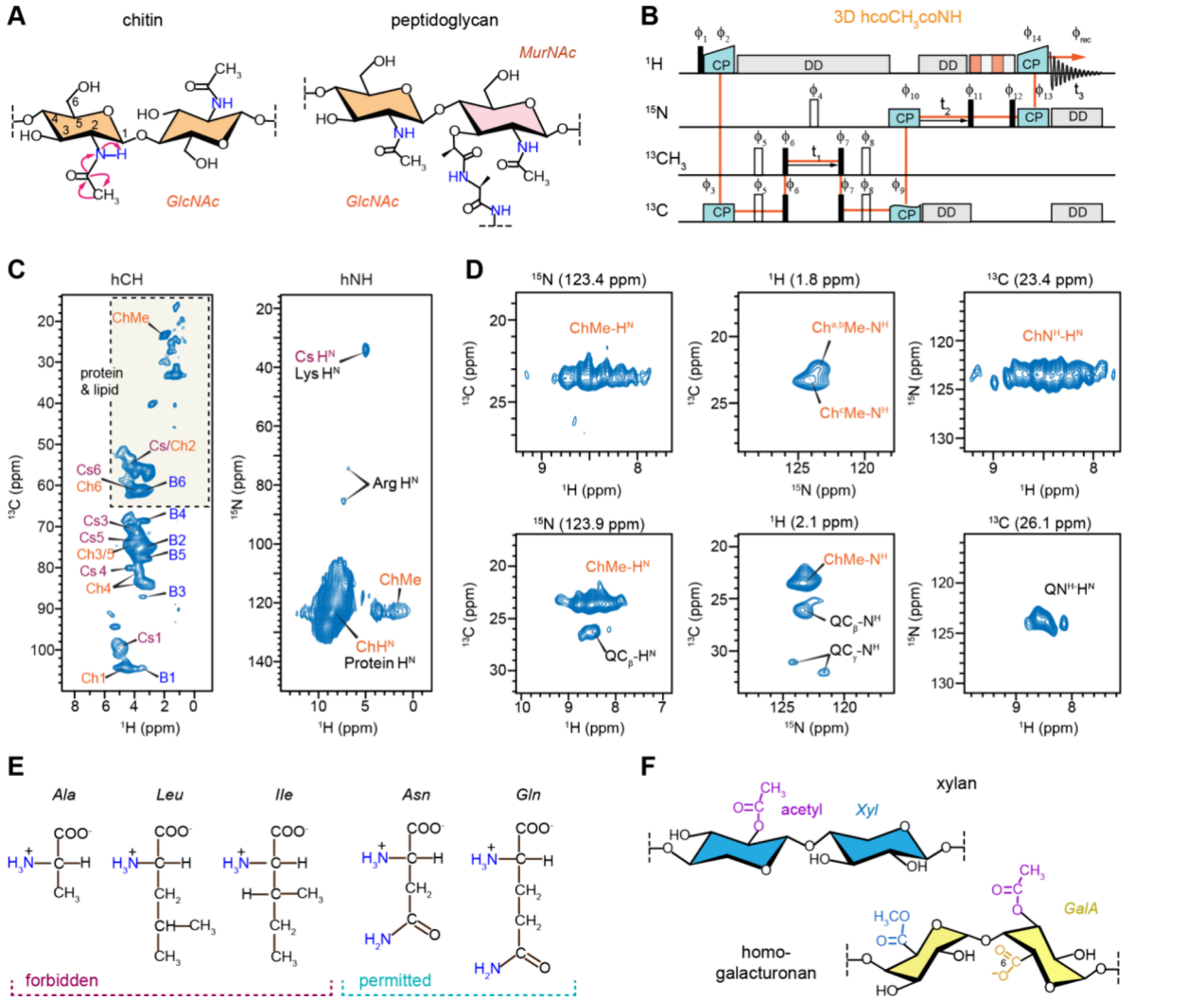

Figure 1. Solid-state NMR analysis of acetyl amino carbohydrates. (A) Simplified representation of fungal chitin and bacterial peptidoglycan containing acetyl amino sugar units (GlcNAc and MurNAc) that will be selected through their $-NH-CO-CH_3-$ segment. The magnetization transfer pathway involving the $-CO-CH_3-NH-$ group in the chitin molecule is depicted. (B) Pulse sequences of 3D hcoCH3coNH experiments that selectively identify acetyl amino carbohydrates by exploiting the $CO-CH_3-CO-NH$ coherence transfer pathway (orange). Magnetization transfer between CO and CH_3 carbons occurs through homonuclear scalar couplings, while heteronuclear dipolar couplings facilitate transfer among ^1H, ^{13}C and ^{15}N. (C) 2D hCH spectrum (left) and hNH spectrum of a pathogenic fungus *R. delemar* display signals corresponding to carbohydrates, proteins, and lipids. These signals exhibit significant overlap, as highlighted by the dashed-line box in the hCH spectrum and the amide H^N signal originating from both chitin and protein. (D) 2D planes extracted from the 3D hcoCH3coNH spectrum of *R. delemar* reveal the well-resolved signals of chitin alone (top panels) along with signals of Gln (bottom panels). The structural polymorphism of chitin is best evidenced by the multiplicity observed for ChMe-H^N and ChN^H-H^N cross peaks. (E) Signals from most amino acids, e.g., Ala, Leu, and Ile, will be filtered out due to the lack of the $-NH-CO-CH_3-$ segment, while Asn and Gln may show up in the spectra due the presence of the $-CO-CH_2-NH-$ segment in the side chain, where the $-CH_2-$ chemical shift can be similar to $-CH_3-$. (F) When modified by eliminating the last step of polarization transfer to NH, this experiment can also be used to select acetylated carbohydrates such as xylan and pectin (e.g., homogalacturonan) in plants. Spectra were measured on an 800 MHz spectrometer using a 1.3 mm probe at 60 kHz MAS. The cooling gas temperature was set to 250 K, with an approximate sample temperature of 302 K.

302 K under 60 kHz MAS, with a possible deviation of a few degrees Celsius, and thus remained at ambient temperature.

The rigid molecules of all fungal samples were initially screened using 2D hCH and hNH experiments. Selective detection of acetyl amino sugars was achieved using a 3D hcoCH3coNH experiment, which incorporated two spin-echo periods to allow magnetization transfer via scalar coupling between $CO-CH_3$ and CH_3-CO, with a half-echo period set to 4.7 ms.[44] During this experiment, the spectral carrier was set to the carbonyl (CO) region (170 ppm) by using an offset during the first CP step. Following this, the offset was changed to the CH_3 region (20 ppm), where CH_3 carbon chemical shifts evolved during t_1 evolution. Magnetization was subsequently transferred back to the directly bonded CO via scalar coupling followed by selective CO-N transfer using the CN-CP step. During this step, magnetization was transferred from CO to ^{15}N using a constant-amplitude radio frequency field of 25 kHz on ^{15}N and a tangent-modulated spin-lock field of 35 kHz on ^{13}C, with an optimized CP contact time of 8 ms.

Nonacetyl amino sugars were selectively detected using a 2D hc_2NH experiment, where selective magnetization transfer from C2 to N was achieved via specific CP with a contact time of 3 ms at 15 kHz MAS. Intermolecular interactions happening between different rigid biopolymers were investigated using 2D hChH with RFDR (radio frequency-driven recoupling) where the RFDR-XY8 recoupling period was varied from 33 μs to 0.8 ms.[110,111]

The mobile matrix was detected by using two experimental schemes. The 3D hCCH-TOCSY (total correlation spectroscopy) experiment

https://doi.org/10.1021/jacs.5c04054
J. Am. Chem. Soc. 2025, 147, 17416−17432

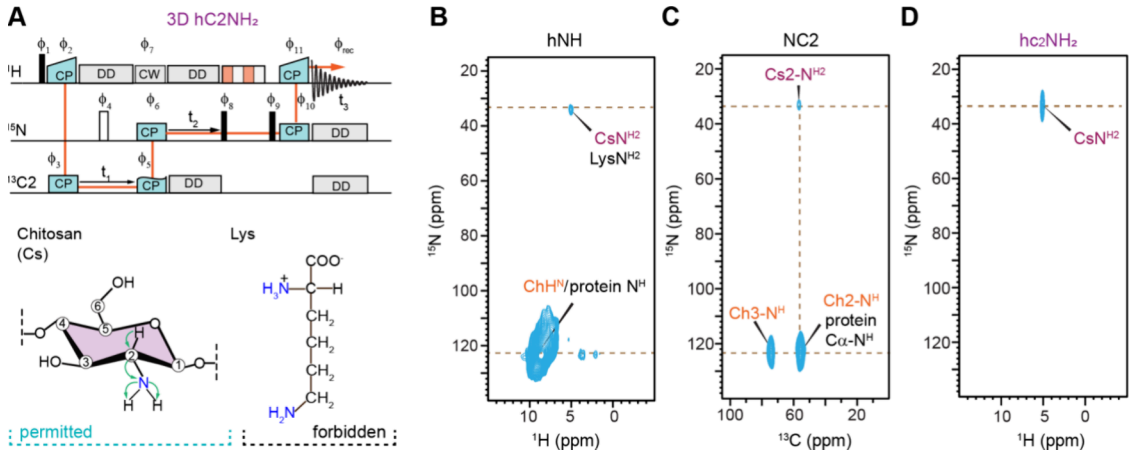

Figure 2. Selective detection of chitosan in protonated $^{13}C,^{15}N$-labeled *R. delemar*. (A) Selective detection of chitosan can be achieved using the $hC2NH_2$ experiment, with the pulse sequences shown in the top panel and with the magnetization transfer pathway highlighted. This is achieved through the C2−N−H_2 segment of chitosan (bottom panel). Lysine has a similar C_ε−N−H_2 segment but will be filtered out in this experiment. (B) 2D hNH spectrum illustrates the overlap of chitosan and lysine amine resonances, alongside chitin and protein amide resonances. (C) The 2D NC2 spectrum, obtained with a ^{13}C offset at 55.4 ppm and selective transfer to ^{15}N at 33.6 ppm, highlights specific signals for chitosan. The lysine NH_2−C_ε cross peak is absent. Chitin C2-protein signals are also observed, although protein amides may overlap with chitin resonances around 55.4 ppm. (D) The 2D hc2NH2 spectrum emphasizes the selective detection of chitosan amine resonances by transferring magnetization from ^{15}N at 33.6 ppm to ^{1}H, effectively suppressing all protein signals and chitin signals, which are well outside the selectively excited region.

employed WALTZ-16 (wideband alternating-phase low-power technique for zero-residual splitting) mixing for carbon−carbon through-bond connectivity using a 15 ms mixing period.[39,112] Conversely, the 3D *J*-hCCH-TOCSY experiment utilized DIPSI-3 (decoupling in the presence of scalar interactions) mixing for 25.5 ms to enhance carbon−carbon connectivity within the mobile regions of the cell wall.[90] Through-bond $^{1}H-^{13}C$ correlations were analyzed using 2D refocused *J*-INEPT-HSQC (insensitive nuclei enhanced by polarization transfer−heteronuclear single quantum coherence) with a *J*-evolution period of 2 ms.[90,113]

To investigate molecular dynamics, relaxation filter and dipolar dephasing methods were employed, including ^{13}C-T_1-filtered 2D hCH and ^{1}H-$T_{1\rho}$-filtered $^{1}H-^{15}N$ HETCOR experiments, utilizing frequency-switched Lee−Goldburg (FSLG) sequences for homonuclear dipolar decoupling.[114] ^{13}C R_1 relaxation rates were measured using a 2D hCH experiment, incorporating a $\pi/2$−delay−$\pi/2$ sequence before the t_1 evolution period, with the delay systematically varied across a series of experiments. Similarly, ^{13}C $R_{1\rho}$ rates were determined using a 2D hCH experiment, where a spin-lock pulse was applied before t_1 evolution and the delay was incremented over a series of measurements.

For these 2D and 3D experiments, a $\pi/2$ pulse was applied with an rf field strength of 100 kHz on ^{1}H, 50 kHz on ^{13}C, and 35.7 kHz on ^{15}N. Initial cross-polarization (CP) transfer from ^{1}H to $^{13}C/^{15}N$ was performed under double-quantum (DQ) CP conditions utilizing an rf field amplitude of 40−50 kHz on ^{1}H and 10−20 kHz on $^{13}C/^{15}N$. To probe both short- and long-range correlations, the second CP contact time was varied between 50 μs and 2.5 ms at 60 kHz MAS. For all proton-detection measurements, slpTPPM (swept low power two-pulse phase modulation) decoupling was applied to the ^{1}H channel with an rf field strength of 10 kHz.[115] During ^{1}H acquisition, WALTZ-16 decoupling was applied to the ^{13}C and ^{15}N channels, also with an rf field strength of 10 kHz.[112] In ^{13}C and ^{15}N detection experiments, the SPINAL-64 (small phase incremental alteration with 64 steps) heteronuclear dipolar decoupling sequence was applied to the ^{1}H channel with an rf field strength of 80 kHz.[116] Water signal suppression was achieved using the MISSISSIPPI (multiple intense solvent suppression intended for sensitive spectroscopic investigation of protonated proteins) sequence.[117] Data acquisition was performed using the States-TPPI method,[118] and the acquired data were processed with Topspin version 4.2.0.

RESULTS AND DISCUSSION

Selective Detection of Acetyl Amino Sugars and Other Acetylated Carbohydrates. Acetylated polysaccharides are ubiquitous across nearly all living organisms, exhibiting highly diverse acetylation patterns that influence their chemical and conformational structures, as well as their biological activities, including immunomodulatory and antioxidant properties.[100,101] Among these, acetyl amino sugars—such as *N*-acetylglucosamine (GlcNAc), *N*-acetylgalactosamine (GalNAc), *N*-acetylmuramic acid (MurNAc), and *N*-acetylneuraminic acid (NeuNAc)—are key components of structural polysaccharides, glycosphingolipids, and glycoproteins. They play critical roles in microbial cell walls, including chitin and galactosaminogalactan in fungi and peptidoglycan in bacteria, which contribute to mechanical strength (Figure 1A).[5,119] In mammals, sialic acids, predominantly NeuNAc, are abundant on cell surfaces and are crucial for regulating cellular communication.[102] However, within complex cellular environments, the spectral signals of acetyl amino sugars overlap significantly with those of other carbohydrates and proteins, making their selective detection challenging.[120]

To address this issue, we developed the 3D $hcoCH_3coNH$ experiment by modifying the 3D coCAcoNH pulse sequence widely applied for protein backbone resonance assignment[44] to selectively detect acetyl amino sugars through the CO−CH_3−CO−NH polarization transfer pathway across their characteristic −NH−CO−CH_3− segments (Figure 1B). The effectiveness of this approach is demonstrated using the mycelia of the pathogenic fungus *R. delemar*, where conventional 2D hCH spectra showed heavy overlap of chitin methyl (ChMe) and carbon 2 (Ch2) signals with protein and lipid peaks, while other chitin carbons mixed with β-glucan and chitosan signals (Figure 1C and Table S5). Furthermore, the amide signals of chitin (ChH^N) were indistinguishable from those of protein backbone amides in standard spectra. In contrast, the $hcoCH_3coNH$ spectrum clearly distinguished chitin-specific signals, such as the ChMe-H^N cross peaks between the chitin methyl carbon and

https://doi.org/10.1021/jacs.5c04054
J. Am. Chem. Soc. 2025, 147, 17416−17432

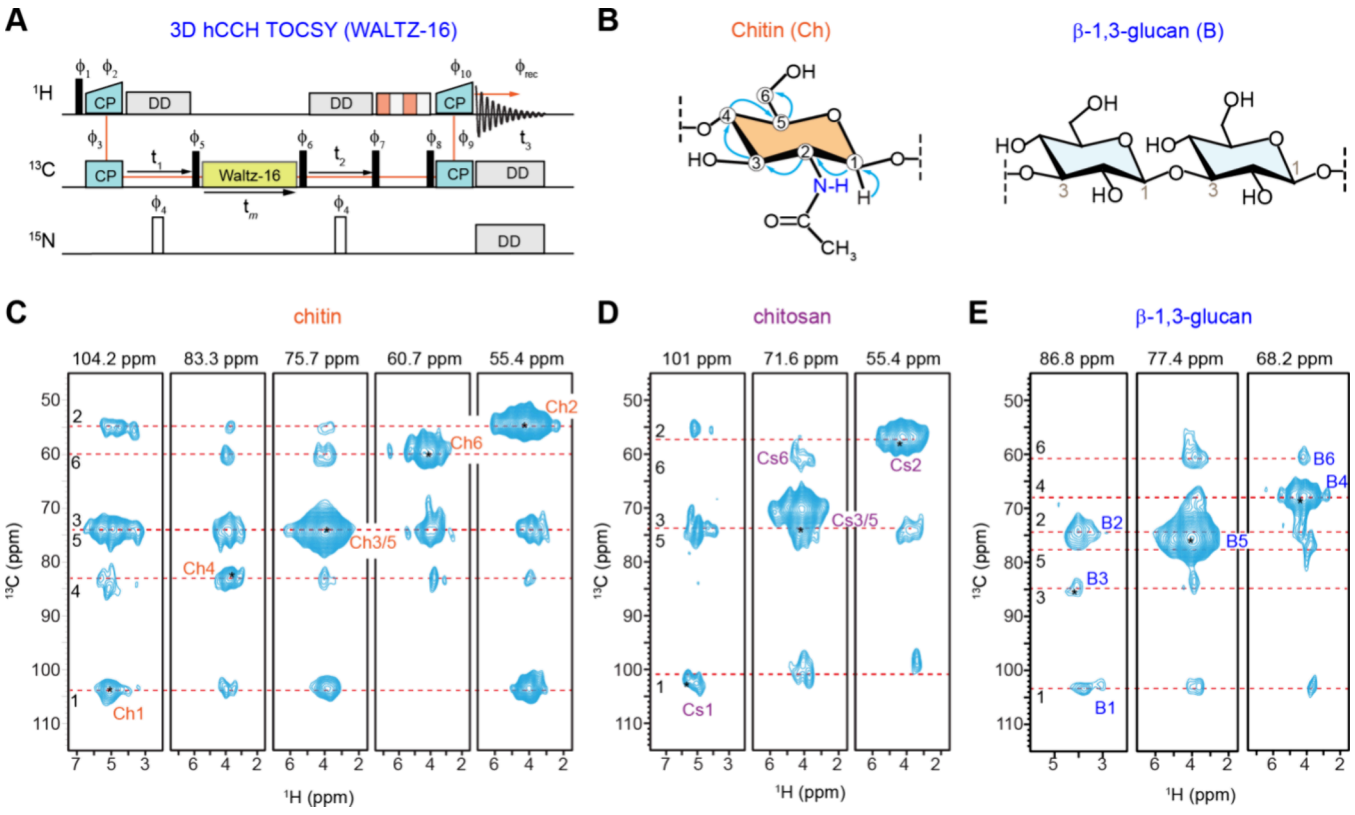

Figure 3. Establishing through-bond and through-space correlations in protonated *R. delemar*. (A) Pulse sequences of 3D hCCH TOCSY with WALTZ-16 mixing, which can be used to map carbon connectivity within each carbohydrate component, relying on scalar couplings among ^{13}C nuclei. 2D strips extracted from a 3D hCCH TOCSY spectrum measured on *R. delemar* with a mixing time of 15 ms are shown for (B) chitin, (C) chitosan, and (E) β-1,3-glucan, capturing multibond correlations across six carbons sites within each monosaccharide unit. All spectra were collected on a 600 MHz NMR spectrometer at 60 kHz MAS.

amide proton and the ChN-H^N cross peak between nitrogen and amide protons (Figure 1D).

A high degree of structural polymorphism has been reported in fungal chitin, mostly relying on ^{13}C NMR, with *A. fumigatus* typically exhibiting three to four distinct chitin forms, while the chitin-rich *Rhizopus* and *Mucor* species display four to eight forms.[32,94,121] The molecular basis of this polymorphism remains unclear, potentially arising from variations in conformation, hydrogen bonding patterns in chitin crystallites, and the complexity of chitin biosynthesis. While yeasts such as *Candida* and *Saccharomyces* possess 3 to 4 chitin synthase (CHS) genes belonging to families I, II, and IV, filamentous fungi like *Aspergillus* and *Rhizopus* harbor between 9 and 23 CHS genes[115−117]. The high resolution of ^1H allowed for the differentiation of up to 15 features in the ChN-H^N signals, with the amide ^1H chemical shift spanning from 7.8 to 9.2 ppm (Figure 1D), providing a foundation for future studies on chitin biosynthesis by analyzing single-knockout mutants of chitin synthase.

It should be noted that despite the selective filtering of amino acids lacking the −NH−CO−CH_3− structural motif, some glutamine (Gln, Q) signals, such as QCβ-H^N and QCγ-H^N, persist in the spectra (Figure 1D). This occurs when their side chain CH_2 chemical shifts are close to those of methyl groups, allowing for the CO−CH_2−CO−NH_2 transfer pathway across their CH_2−CO−NH_2 segment (Figure 1E). However, their $^{13}C\beta$ and $^{13}C\gamma$ chemical shifts, typically at 26 and 32 ppm, respectively, remain spectroscopically distinct from chitin signals, minimizing interference (Figure 1D).

This experimental approach can be further adapted to detect other acetyl amino sugars, including GalNAc in fungal galactosaminogalactan, GlcNAc and MurNAc in bacterial peptidoglycan, and NeuNAc in mammalian sialic acids. Additionally, by omitting the final step of the polarization transfer pathway, a variant h$COCH_3$ experiment can be used to selectively detect all acetylated carbohydrates in the cell. This includes acetylated galacturonic acid (GalA) in pectin, which regulates plant growth and stress responses, and acetylated xylose (Xyl) in xylan, which modulates xylan folding on cellulose microfibrils, thereby impacting the structure of mature lignocellulose (Figure 1F).[25,26,122] These applications highlight the potential of this method for investigating the structural and functional roles of acetylation in diverse biological systems.

Selective Detection of Nonacetyl Amino Sugars. The second experiment, hc2NH_2, inspired by the CαNH experiment commonly used for protein backbone intraresidue assignments, has been specifically designed for the detection of nonacetyl amine sugars such as glucosamine (GlcN) and galactosamine (GalN). For instance, chitosan, produced from chitin by enzymes named chitin deacetylase (CDA), consists of GlcN units that lack the $COCH_3$ motif (Figure 2A), making its identification particularly challenging due to significant spectral overlap between the ^{15}N and ^1H signals of chitosan amines (NH_2) and those of lysine side chains in proteins. In particular, ^{15}N resonances around 120 ppm are associated with both chitin and proteins, whereas the peak at 33.6 ppm corresponds to both chitosan and lysine (Figure 2B). Although chitosan and lysine exhibit similar ^{15}N (33.6 ppm) and ^1H (5.0 ppm) chemical

https://doi.org/10.1021/jacs.5c04054
J. Am. Chem. Soc. 2025, 147, 17416−17432

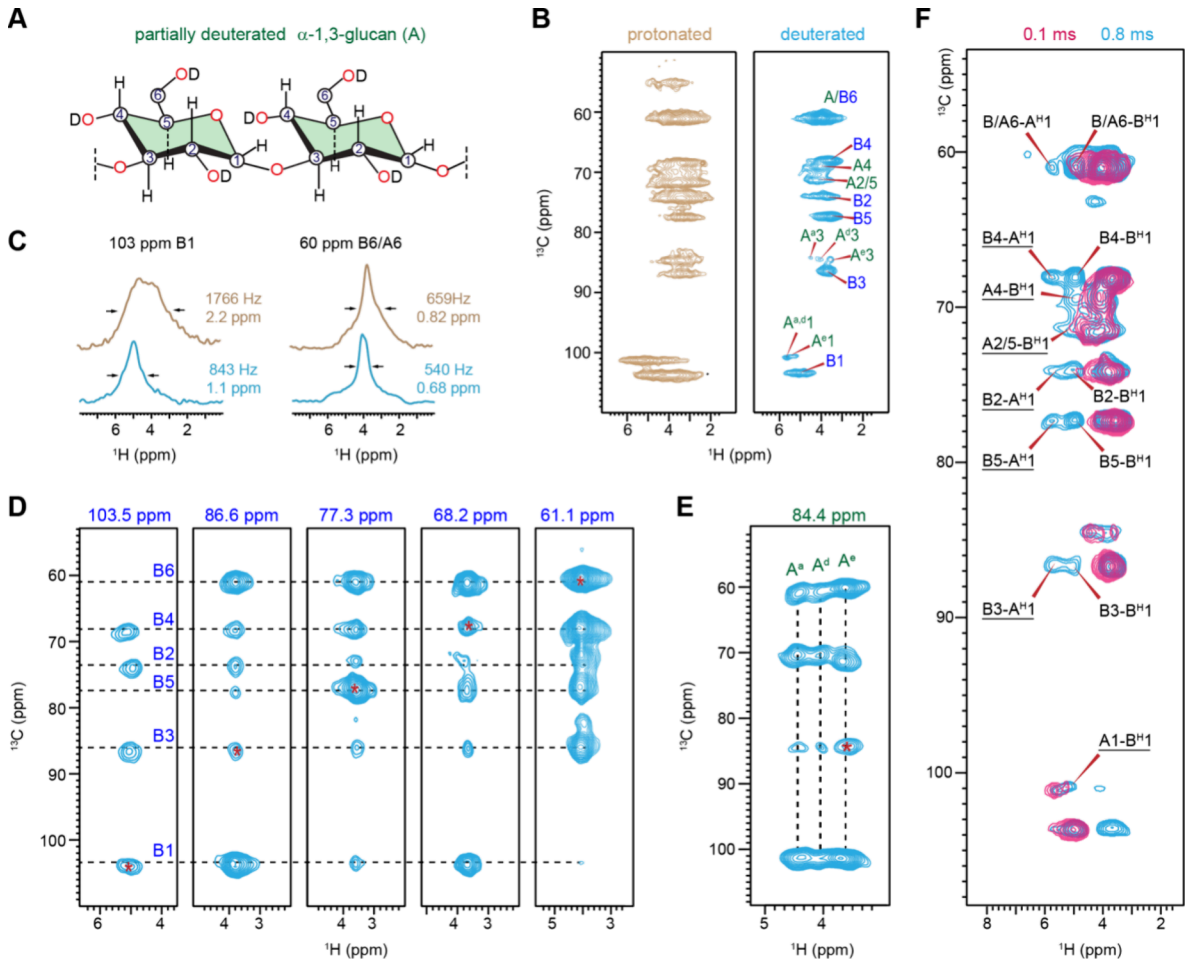

Figure 4. Deuteration of *A. fumigatus* cell walls for enhancement of ^{1}H resolution. (A) Structural representation of a deuterated α-1.3-glucan. (B) Two-dimensional hCH spectra of rigid carbohydrates in fully protonated (brown) and deuterated (blue) *A. fumigatus* mycelia. A short 50 μs contact time was used for the second CP to partially reduce ^{1}H−^{1}H spin diffusion. (C) Comparison of ^{1}H line widths extracted from 2D hCH spectra of protonated (brown) and deuterated (blue) *A. fumigatus* mycelia. (D) Two-dimensional planes extracted from 3D hCCH TOCSY spectrum of deuterated *A. fumigatus* mycelia with a WALTZ-16 mixing period showing through-bond ^{13}C−^{13}C connectivity of rigid β-1,3-glucans. (E) Polymorphic forms (A^a, A^d, and A^e) of α-glucans identified from the strip of the same 3D hCCH TOCSY spectrum. (F) Intermolecular interactions between α- and β-1,3-glucans resolved using 2D hChH spectra with different RFDR mixing times measured on deuterated *A. fumigatus* mycelia. Unambiguous intermolecular cross peaks between α- and β-glucans are underlined. The spectra were acquired on a 600 MHz spectrometer with an MAS rate of 60 kHz.

shifts, their ^{13}C chemical shifts are markedly different, with lysine's NH_2-attached $^{13}C\varepsilon$ resonating between 30 and 40 ppm, while chitosan's C2 carbon resonates at 55 ppm. This distinction enables the selective detection of chitosan using a 2D ^{15}N−^{13}C correlation experiment, wherein magnetization is transferred from ^{13}C at 55 ppm to ^{15}N at 33.6 ppm, thereby unambiguously identifying chitosan signals (Figure 2C). The cross-polarization conditions optimized for ^{13}C at 55 ppm also capture chitin carbon signals that correlate with ^{15}N at 124 ppm; however, lysine's NH_2−Cε correlation is absent. Furthermore, in the hc2NH_2 spectrum, chitin signals are effectively eliminated by transferring magnetization only from the ^{15}N site of 33.6 ppm to ^{1}H, ensuring that only chitosan signals are observed (Figure 2D). In addition to fungal chitosan, it is important to note that nonacetylated amino sugars, such as GlcN and MurN, are also abundant in the peptidoglycan of most Gram-positive bacterial species, contributing significantly to their resistance to lysozyme.[123] This method can be broadly applied to investigate the structure of nonacetyl amino sugars across various organisms and species.

Connectivity and Polymorphism in Rigid Polysaccharides of Protonated and Deuterated Cells. The 3D hCCH TOCSY experiment with a 15 ms WALTZ-16 mixing time (Figure 3A), typically used for side chain assignment in proteins,[124] was employed to precisely map through-bond carbon connectivity in rigid polysaccharides (Figure 3B). When applied to fully protonated *R. delemar* cell walls under moderate magnetic field strength and MAS rate (600 MHz or 14.4 T, and 60 kHz), it allowed for the tracing of the complete six-carbon backbone connectivity of chitin, chitosan, and β-glucan (Figure 3C−E). Structural polymorphism, reflected by peak multiplicity, was observed for all chitin carbons, with the ^{1}H2 chemical shift ranging from 3 to 5.5 ppm (Figure 3C). A similar peak multiplicity was noted for chitosan, where the ^{1}H2 ranged from 2.5 to 5.5 ppm, revealing multiple resolvable peaks (Figure 3D). Although ^{1}H T_2 relaxation can contribute to line broadening, the peak multiplicity observed for chitin and chitosan is primarily due to structural polymorphism with relaxation effects playing a lesser role. The signals did not show the characteristic pattern of homogeneous broadening typically caused by relaxation.

https://doi.org/10.1021/jacs.5c04054
J. Am. Chem. Soc. 2025, 147, 17416−17432

Instead, discrete peaks can be resolved, such as the multiple C2 peaks in the 104.2 ppm strip for chitin. Furthermore, chitin and chitosan exhibit a higher degree of peak multiplicity than β-glucan even though all three components are present in the same fully protonated sample. Although β-glucan is a minor component in the *R. delemar* cell wall, accounting for only 5% of the rigid polysaccharides, its complete carbon connectivity was still observable (Figure 3E). This approach not only enables the tracking of carbon connectivity but also provides insight into the structural polymorphism of rigid polysaccharides.

However, we were dissatisfied with the spectral quality. For instance, the ^{1}H lines were extremely broad, which were unacceptable for biomolecular NMR structural characterization. Additionally, we observed that in some regions, not all carbon connectivity was detected in the 2D strips. This could be due to unaveraged ^{1}H−^{1}H dipolar couplings, which may attenuate the signal during TOCSY mixing, as proton decoupling cannot be applied during the mixing period. To address these challenges, we deuterated the fungal cells, drawing inspiration from the protocol used in protein proton solid-state NMR studies, where backbone amides in perdeuterated proteins are back-exchanged to protons, and the proton dilution leads to resolution enhancement.[36,125]

To optimize the protocol, we turned to a different pathogenic fungal species, *A. fumigatus*, whose genome and carbohydrate structure are well characterized, thus serving as a more suitable model system.[126] The fungus was trained to grow in deuterated media with the D_2O concentration gradually increased by 10% at each step, from 10 to 100%, until the fungi were able to grow in fully deuterated media without exhibiting any stressed phenotype. Since the ^{13}C-glucose and ^{15}N-sodium nitrate used in the medium for carbohydrate biosynthesis are protonated, the cell wall carbohydrates were synthesized in a fully protonated state, preserving ^{13}C-bound protons necessary for structural analysis, while protons at exchangeable sites, such as hydroxyl (−OH) and amide and amine (−NH and $-NH_2$) groups, were replaced by deuterons (Figure 4A). Considering the structure of long glucans, such as α-1,3-glucan, this protocol should decrease the proton density by approximately 30% due to the replacement of three −OH groups with −OD groups while maintaining the remaining seven CH sites intact within each sugar unit along the glucan chain.

Partial deuteration and proton dilution significantly improved the ^{1}H resolution, as demonstrated by the overlay of 2D hCH spectra measured on deuterated and protonated mycelia of *A. fumigatus* (Figure 4B). The three allomorphs of α-1,3-glucans became distinguishable in the deuterated samples, as reflected by three resolvable peaks corresponding to their H3−C3 cross peaks (A^a3, A^d3, and A^e3), with ^{13}C resonating at 84 ppm and ^{1}H chemical shifts of 4.4 4.1, and 3.6 ppm. The 1D ^{1}H cross sections extracted from the 2D spectra indicated that the ^{1}H lines were narrowed by one-fourth to one-half due to partial deuteration (Figure 4C and Figures S3 and S4). This significant effect likely arises from the combination of three mechanisms: first, a direct impact due to diminished ^{1}H−^{1}H homonuclear dipolar couplings; second, the removal of contributions from hydroxyl proton signals; and third, a decrease in ^{1}H spin diffusion caused by lower ^{1}H density, which enhances site specificity for each ^{13}C−^{1}H cross peak in the 2D spectrum. Even with the use of a short 50 μs contact time in the second CP to increase site specificity during the final step of polarization transfer in the hCH experiment, ^{1}H spin diffusion still occurred efficiently, contributing to the detection of remote ^{1}H resonances and broadening the lines.

The application of the same 3D hCCH TOCSY with WALTZ-16 mixing to partially deuterated *A. fumigatus* cells enabled us to unambiguously trace the carbon connectivity in rigid β-1,3-glucans (Figure 4D) and, more importantly, resolved the complete carbon connectivity of three new allomorphs of α-1,3-glucans, named A^a, A^d, and A^e (Figure 4E and Table S6). These α-1,3-glucan forms shared identical ^{13}C chemical shifts but exhibited significantly varied ^{1}H chemical shifts. In previous studies of *A. fumigatus*, these three ^{1}H-identified allomorphs showed only a single set of ^{13}C peaks and were labeled as A^a, which displayed distinct ^{13}C chemical shifts from the other two forms of α-1,3-glucans (A^b and A^c).[107] By combining the ^{1}H and ^{13}C resolution, we are now able to resolve a total of five forms of α-1,3-glucans, each exhibiting structural variations.

We are now able to evaluate the structural functions of these α-1,3-glucans by combining chemical shift information and the origin of their signals in *A. fumigatus* cultures prepared under different conditions. The consistent ^{13}C signals of A^a, A^d, and A^e represent the primary structure of α-1,3-glucan predominantly found in the rigid portion of the mycelial cell walls, consistently observed in multiple strains of *A. fumigatus* as well as other *Aspergillus* species, such as *A. nidulans* and *A. sydowii*.[93,107,108] Therefore, A^a, A^d, and A^e form the rigid domain of *Aspergillus* cell walls by associating with chitin and a small portion of β-glucans, with variations of local structures leading to their varied ^{1}H chemical shifts. In contrast, A^b and A^c have fully altered helical screw conformations, as evidenced by a distinct ^{13}C chemical shift for their C3 sites, observed in the mobile fraction of *A. fumigatus* cell walls at very low concentrations. However, their abundance became considerable in both the rigid and mobile phases of *A. fumigatus* mycelia grown under exposure to echinocandins, an antifungal drug that inhibits β-1,3-glucan biosynthesis.[107] The coexistence of three different helical screw structures with stress responses may be linked to the biosynthetic complexity arising from the presence of multiple α-glucan synthase (AGS) genes in *A. fumigatus*, a topic for the next study, likely by connecting NMR with *ags* mutants.[127] However, it is clear that the availability of five structural forms allows α-1,3-glucans to play crucial roles as buffering molecules by supporting the rigid core through interaction with chitin microfibrils and regenerating the matrix when β-1,3-glucans are depleted due to echinocandin antifungal treatment.

We also identified seven unambiguous intermolecular cross peaks between α-1,3-glucan and β-1,3-glucan by comparing two 2D hChH spectra measured on the partially deuterated sample with varying RFDR mixing periods of 0.1 and 0.8 ms (Figure 4F). Extending this experiment to a 3D format by adding an additional ^{1}H dimension will enable us to further differentiate the various structural forms of α-1,3-glucan and evaluate their specific interactions with β-1,3-glucans, providing insights into polymer packing at the subnanometer length scale within the cell wall architecture. It is exciting that such a task has now become feasible using moderate magnetic field strength and MAS frequency, within just a few hours, while working with intact cells.

Resolving the Structural Complexity of Mobile Carbohydrates. A characteristic feature of the extracellular matrix in living organisms is its heterogeneous dynamics, wherein polymers are distributed across distinct dynamic domains. This organization typically consists of a rigid core that provides structural stiffness surrounded by a more mobile

https://doi.org/10.1021/jacs.5c04054
J. Am. Chem. Soc. 2025, 147, 17416−17432

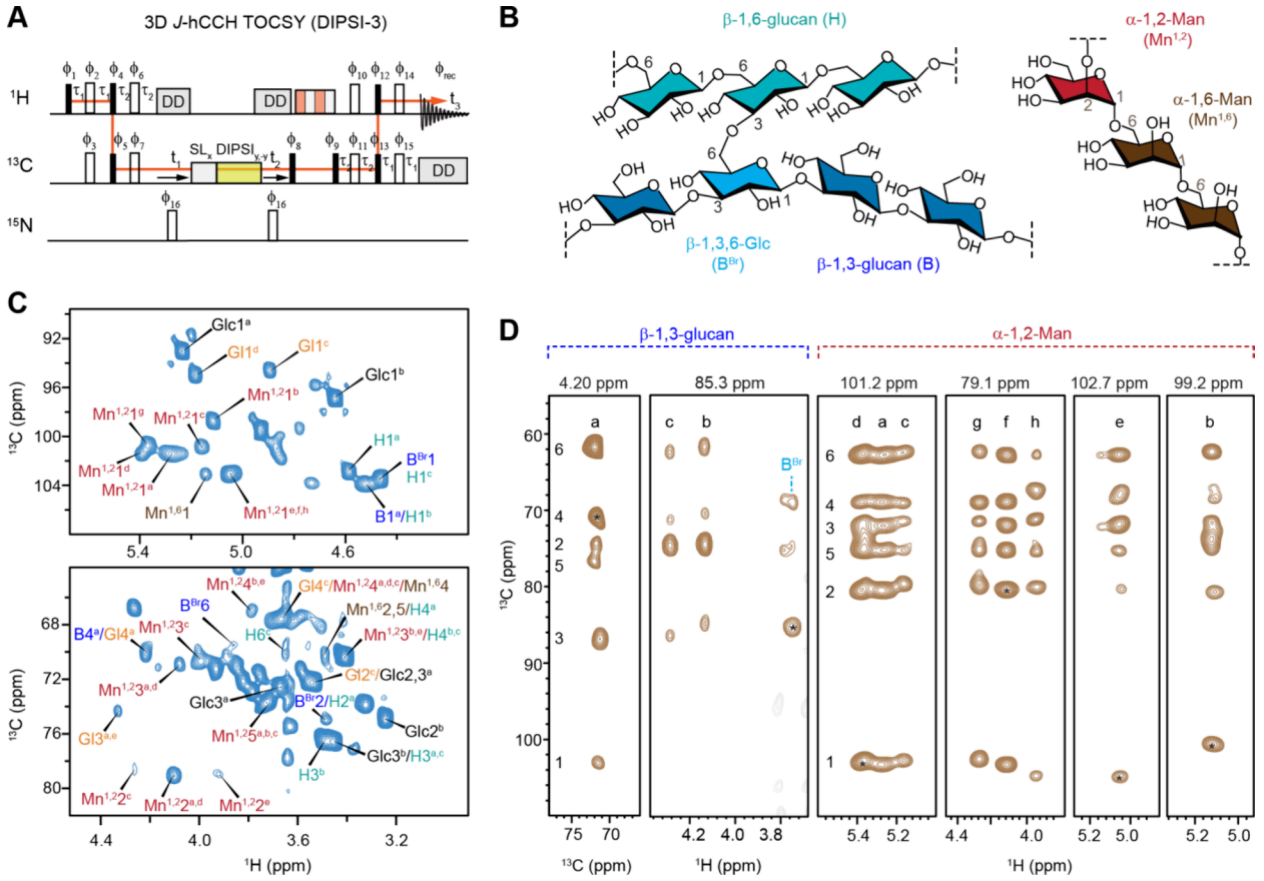

Figure 5. Resonance assignment of mobile carbohydrates in protonated *C. albicans*. (A) Pulse sequences of 3D hCCH TOCSY with DIPSI-3 mixing for establishing through-bond carbon connectivity in mobile carbohydrates. (B) Simplified representation of segments in the β-glucan matrix (left) and mannan (right) of *C. albicans* cell walls. (C) Selected regions of the 2D hcCH TOCSY (DIPSI-3) spectrum. (D) Extracted 2D stripes from the 3D hCCH TOCSY (DIPSI-3) spectrum resolving three types of β-1,3-glucan (types a, b, and c) alongside β-1,3,6-linked Glc site for branching, as well as eight types of α-1,2-linked Man residues in mannan. The 2D C−C strips were extracted at the proton sites, whereas 2D C−H strips were extracted at the carbon sites. The chemical shifts labeled at the top of each panel represent the ^{1}H or ^{13}C site where strips are extracted, and asterisks indicate the corresponding diagonal peak. The experiments were performed on an 18.8 T (800 MHz) spectrometer with 15 kHz MAS.

matrix. In the fungal cell wall, for instance, chitin and chitosan predominantly contribute to the rigid fraction, while certain polysaccharides, such as α- and β-glucans and mannan, are present in both rigid and mobile phases.[128] Meanwhile, exopolysaccharides, such as galactosaminogalactan, are exclusively found in the mobile fraction. Recent studies have leveraged advanced NMR techniques to investigate these dynamic domains. Baldus and colleagues utilized a proton-detected 3D ^{1}H−^{13}C *J*-hCCH-TOCSY (DIPSI-3) experiment (Figure 5A) to assign protein signals and identify the reducing ends of glycans in *S. commune*.[90] Inspired by their pioneering work, we have recently applied this approach to characterize the mobile regions of the cell walls in a multidrug-resistant fungus named *Candida auris*, enabling the precise identification of mannans and glucans in their mobile matrix.[95] Loquet and colleagues have also employed this method to elucidate the organization of mobile capsular polysaccharides in *C. neoformans*.[33]

Here, we highlight the capability of this experiment in resolving the structural polymorphism of mobile matrix polysaccharides using yeast cells of the prevalent pathogen *C. albicans* (strain JKC2830) as a model system. The mobile molecules within this fungus, detected via the 2D hcCH TOCSY (DIPSI-3) spectrum, include linear β-1,3-glucans (B) and β-1,6-glucans (H), which are interconnected through β-1,3,6-linked glucopyranose units (B^{Br}) serving as branching points (Figure 5B,C and Figure S5). Additionally, strong signals from mannan polymers, including the α-1,6-mannan backbone ($Mn^{1,6}$) and α-1,2-mannan side chains ($Mn^{1,2}$), were observed. Signals corresponding to small molecules, such as glucose (Glc) and galactose/glucose derivatives (Gl), were also detected; however, these are not the focus of this discussion, as they are not structural components of the cell wall.

Strips from the F1−F3 plane (^{13}C−^{1}H) of 3D hCCH TOCSY (DIPSI-3) spectra enabled the identification of three distinct forms of β-1,3-glucans (types a, b, and c), as well as the β-1,3−6-linked branching site (Figure 5D), with their chemical shifts documented in Table S7. Our recent analysis revealed that type-a β-1,3-glucan exhibits chemical shifts consistent with those reported for the triple-helix model, suggesting its role in matrix formation. In contrast, type-b β-1,3-glucan displays correlations with chitin, indicating its association with extended structures on chitin microfibrils. The precise structure of type-c remains unknown, but the complete chemical shift data set obtained here can serve as a reference for computational modeling to elucidate its structural origin.

While only a single type of α-1,6-mannan signal was observed, indicating a structurally homogeneous backbone, analysis of the 2D strips extracted at ^{13}C chemical shifts of 101.2, 101.3, 102.7, and 99.2 ppm differentiated eight distinct α-1,2-mannose

https://doi.org/10.1021/jacs.5c04054
J. Am. Chem. Soc. 2025, 147, 17416−17432

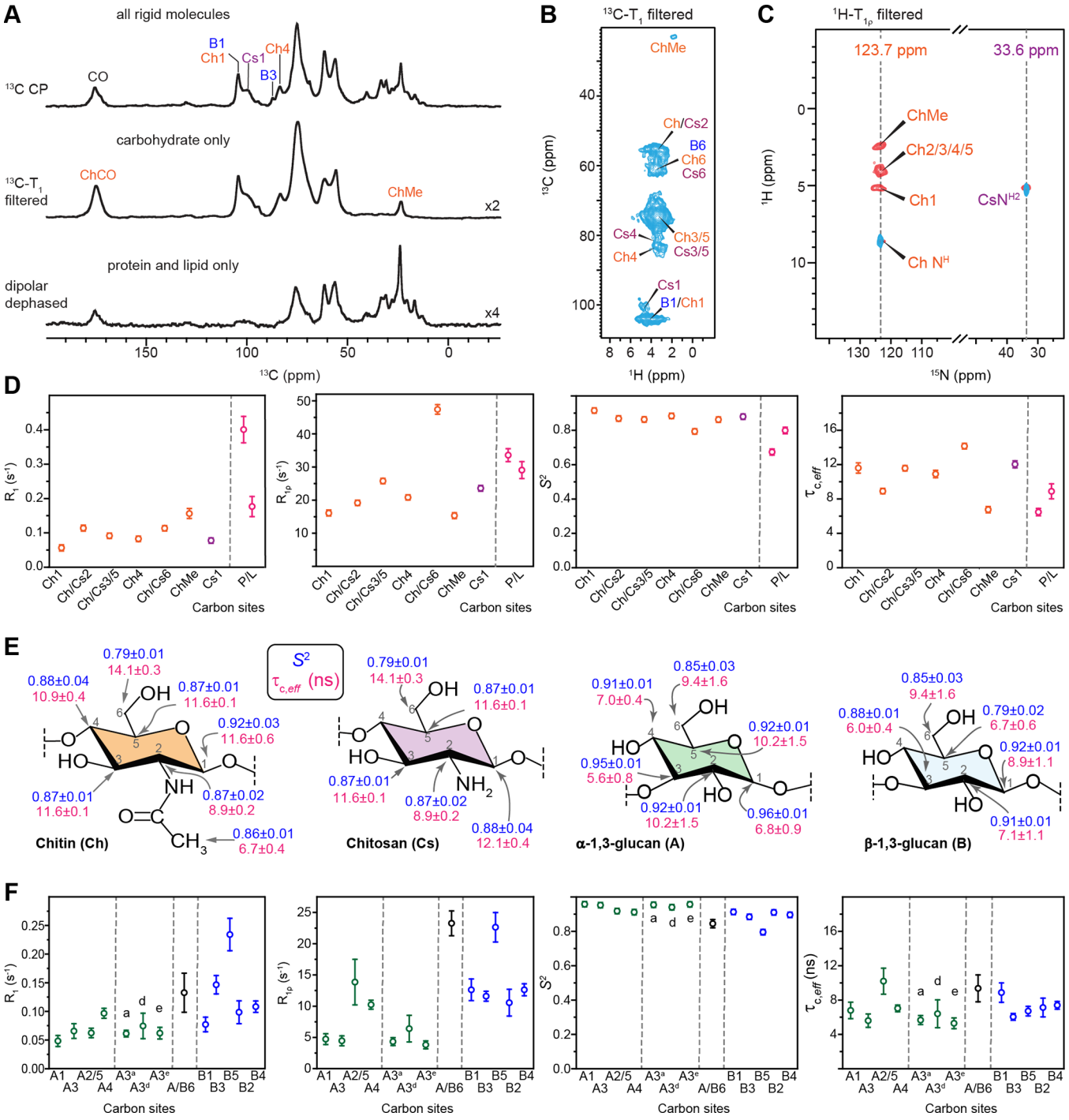

Figure 6. Identifying the rigid and semirigid cell wall components of *R. delemar* and *A. fumigatus*. (A) Three 1D ^{13}C spectra of *R. delemar* using CP for detecting all rigid molecules (top), using ^{13}C-T_1 filter to select cell wall polysaccharides (middle), and using dipolar-dephasing to select proteins and lipids (bottom). (B) ^{13}C-T_1 filtered 2D hCH spectrum retains only signals from rigid cell wall polysaccharides, while all protein and lipid signals are eliminated. (C) Overlay of two ^{1}H $T_{1\rho}$ filtered ^{1}H–^{15}N HETCOR spectra with 2.5 ms (red) and 1.5 ms (blue) CP contact times. (D) Order parameters (S^2) and effective correlation times ($\tau_{C,\,eff}$) determined using analysis of ^{13}C R_1 and ^{13}C $R_{1\rho}$ relaxation rates using a model-free approach are shown for *R. delemar*. Ch: chitin; Cs: chitosan; P/L: protein or lipid. Relaxation experiments were conducted on 600 MHz at 60 kHz MAS. (E) Structural summary of order parameters S^2 (blue) and effective correlation time $\tau_{C,\,eff}$ (magenta). (F) Order parameters (S^2) and effective correlation times ($\tau_{C,\,eff}$) determined for *A. fumigatus* polysaccharides. A: α-1,3-glucan; B: β-1,3-glucan.

($Mn^{1,2}$) structures (Figure 5D). Types a–c could not be distinguished solely by their ^{13}C chemical shifts due to their high degree of similarity, necessitating the use of ^{1}H chemical shifts for effective differentiation. The remaining five types can be readily distinguished by their distinct ^{13}C and ^{1}H chemical shifts at the carbon-1 site. As a major carbohydrate polymer in *Candida* cell walls, mannan forms fibrillar structures extending on the scale of 100 nm, comprising the outer cell wall layer while also penetrating the inner domain to interact with glucans and chitin.[5] The α-1,2-mannose side chains can be covalently linked to the α-1,6-mannan backbone, to other α-1,2-mannose residues along the side chains of varying lengths, and to β-1,2-mannose,

https://doi.org/10.1021/jacs.5c04054
J. Am. Chem. Soc. 2025, 147, 17416–17432

phosphate, or α-1,3-mannose.[129] Recent studies have also identified these side chains as critical interaction sites for mannan fibrils with other polymers, such as glucans and chitin, with these interactions shifting the mannan fibrils from the mobile to the rigid phase under stress conditions.[95] This structural diversity likely accounts for the presence of eight distinct α-1,2-mannose residues in *C. albicans* mannan fibrils. However, the precise assignment of these residues to their structural functions will require the integration of ^{1}H solid-state NMR methodologies with biochemical and genomic approaches.

Dynamics Filters for Separation of Rigid Polysaccharides from Semirigid Proteins. Cellular biomolecules exhibit a broad range of dynamics, prompting the widespread use of relaxation filters to either suppress or detect components with specific motional characteristics. For instance, Duan and Hong recently employed ^{1}H-T_2-filtered hCH and ^{13}C-T_2-filtered INADEQUATE experiments to selectively detect intermediate-amplitude mobile polysaccharides, such as hemicellulose xyloglucan in *Arabidopsis* and surface cellulose and glucuronoarabinoxylan in *Brachypodium*, while suppressing signals from both rigid cellulose and highly mobile pectin.[88] In *R. delemar*, the dipolar coupling-mediated ^{1}H−^{13}C CP-based spectra preferentially enhance signals from partially rigid molecules, revealing a complex mixture of resonances from proteins, lipids, and polysaccharides, including chitin, chitosan, and glucans (Figure 6A). Longitudinal (^{13}C-T_1) relaxation filters with a 10 s delay effectively suppressed signals from semirigid proteins and lipids, preserving only those from rigid cell wall polysaccharides, whereas in the dipolar-dephased spectrum, rigid cell wall polysaccharides are selectively depleted, leaving only protein and lipid signals. It should be noted that the carbonyl and methyl group signals of chitin initially overlapped with those of proteins and lipids in 1D ^{13}C CP spectrum but are unambiguously detected in the protein/lipid-free ^{13}C-T_1-filtered spectrum.

Similar approaches were applied to the 2D hCH spectrum (Figure 6B), where a ^{13}C-T_1 filter effectively suppressed all protein and lipid signals, substantially simplifying the spectrum compared to that in Figure 1C and leaving the ChMe and Ch/Cs2 sites unambiguously resolved. The implementation of a ^{1}H $T_{1\rho}$ filter in a ^{1}H−^{15}N heteronuclear correlation experiment also generated polysaccharide-only spectra, revealing chitin (^{15}N 123.7 ppm) and chitosan (^{15}N 33.6 ppm) signals while depleting protein amide signals (110−130 ppm) and lysine amine signals. These observations have demonstrated that lipids, proteins, and ergosterols reside in the semirigid regime, while cell wall polysaccharides are found in the rigid region of *R. delemar*. The relaxation filters also provide a means to unambiguously visualize cell wall polysaccharides without interference from other molecules.

To determine the order parameters (S^2) of polysaccharides and the effective correlation times of their motions ($\tau_{C,\,eff}$), we fitted ^{13}C R_1 and ^{13}C $R_{1\rho}$ relaxation rates (Figures S6−S9) to a spectral density function, with the rate equations provided in Text S2, and these rates were analyzed using a simple model-free formalism (Text S3). In *R. delemar*, all carbon sites from chitin and chitosan exhibited very slow ^{13}C R_1, ranging from 0.06 to 0.15 s^{-1}, while protein and lipid signals showed faster ^{13}C R_1 between 0.18 and 0.40 s^{-1} (Figure 6D and Table S8), explaining why a clean carbohydrate-only spectrum can be obtained by applying a ^{13}C-T_1 filter. A similar trend was observed for the ^{13}C $R_{1\rho}$, which was slow for most chitin/chitosan sites on the range of 15−25 s^{-1}, except for the most dynamic of chitin carbon 6, whose ^{13}C $R_{1\rho}$ was 47 ± 1 s^{-1}. We noticed that chitin and chitosan exhibit consistent high order parameters ranging from 0.79 to 0.92, with effective correlation times of 10−12 ns for most carbon sites (Figure 6E). This time scale of motion is highly comparable to that observed in microcrystalline β-sheet proteins, where the structurally ordered regions exhibit effective correlation times on the order of tens of nanoseconds.[71,130] In contrast, proteins located in the rigid phase of the cell wall displayed lower order parameters and shorter correlation times of 6−9 ns (Figure 6D and Table S8).

Quantification of their dynamic parameters provided novel insights into the protein−carbohydrate interface in the *R. delemar* cell walls. Recently, we have identified the colocalization of proteins and carbohydrates in this fungus, confirmed through several strong intermolecular cross peaks between isoleucine residues and chitin/chitosan signals within the rigid phase.[94] Chitosan primarily interacted with the isoleucine γ1 site, whereas chitin was positioned on the opposite side, stabilized through contacts with both isoleucine γ1 and γ2 sites.[94] This also enabled the rigid portion of proteins to withstand a prolonged 15 ms proton-assisted recoupling (PAR) period,[131,132] demonstrating their semiordered nature—an observation made for the first time in any fungal species. However, the distinct order parameters and correlation times quantified in this study suggest that bulk-wall-incorporated proteins are not homogeneously integrated with carbohydrates. Instead, despite anchoring through hydrophobic amino acid residues, structured proteins in *R. delemar* cell walls exhibit entirely different dynamic profiles.

The results also provide insight into the colocalization of chitin and chitosan in *R. delemar* cell walls. Since chitosan is generated by chitin deacetylase after chitin microfibrils are deposited into the fungal cell wall,[133] there has been ongoing debate about whether these two polysaccharides coexist within the same polymer (e.g., −GlcN−GlcNAc−GlcN−GlcNAc−) or form separate polymers or structural domains. The comparable effective correlation times of chitosan C1 (12.1 ± 0.4 ns) and chitin C1 (11.6 ± 0.6 ns) suggest that they exist as either structural domains with similar dynamics or are well-mixed within a single polymer chain, rather than existing as distinct polymers with different dynamics (Figure 6E). This structural finding also provides insight into the mode of action of chitin deacetylase.[133]

Extending this approach to partially deuterated *A. fumigatus* provided insights into the functional differences between β- and α-glucans, as well as their polymorphic forms (Figure 6F). α-Glucans exhibited slower ^{13}C R_1 (0.05−0.10 s^{-1}) and $R_{1\rho}$ (4−10 s^{-1}, except for the mixed A2/5 peak), whereas β-glucans displayed faster ^{13}C R_1 (0.08−0.23 s^{-1}) and $R_{1\rho}$ (11−23 s^{-1}). Consequently, α-glucans had noticeably larger order parameters (0.91−0.95) than β-glucans (0.79−0.91), except at the C6 sites, where signal overlap occurred (Figure 6E,F and Table S9). The obtained order parameters are larger than expected for glucans in the matrix. This is likely resulting from partial deuteration, which reduces ^{1}H−^{1}H dipolar couplings, leading to longer relaxation times and longer coherence times and, consequently, higher order parameters.[134] Future efforts should explore incorporating dipolar coupling data and relaxation measurements into the SMF analysis to achieve more accurate determination of order parameters for carbohydrates.[75] Overall, the observed trend aligns with structural concepts established through solid-state NMR, particularly the observation of intermolecular interactions, reinforcing that α-1,3-glucan—rather than β-1,3-glucan—is the key component physically

https://doi.org/10.1021/jacs.5c04054
J. Am. Chem. Soc. 2025, 147, 17416−17432

packed with chitin microfibrils in *A. fumigatus* mycelial cell walls. Additionally, the three rigid α-1,3-glucan forms ($A3^a$, $A3^d$, and $A3^e$), distinguishable by their ^1H chemical shifts at the C3 site, exhibited similar structural properties, with consistent order parameters of 0.95−0.98 and effective correlation times of 4.5−5.0 ns (Figure 6F). This confirms our hypothesis that these coexisting forms share only local structural variations within the rigid α-1,3-glucan domain, in contrast to the dynamically distinct $A3^b$ and $A3^c$ forms, which are implicated in biosynthetic differences and stress-compensatory mechanisms.[107]

Revisiting the Carbohydrate Structure and Assembly in Fungal Cell Walls. The results provide novel insights into the structural and functional complexity of cell wall polysaccharides in three prevalent pathogenic fungal species. One key finding pertains to the structural complexity of chitin and its association with chitosan and proteins. A previous ^{13}C, ^{15}N-based solid-state NMR study of *R. delemar* and several other *Rhizopus* and *Mucor* species revealed a shared structural organization across these species.[94] This includes four types of chitin and four types of chitosan, along with a minor contribution (5%) of β-1,3-glucan, which together form the rigid domain. This rigid structure is supported by a softer matrix composed of galactan- and mannan-based polysaccharides as well as α-poly fucoses. High-resolution ^1H data of *R. delemar* from this study revealed that chitin is even more complex than previously observed, with up to 15 peaks for the amide ^1H of chitin. This indicates a broad range of conformational distributions and hydrogen-bonding patterns,[121] necessitating follow-up studies to explore the biochemical and structural origins of this polymorphism. We also found that structural proteins complexed with chitin and chitosan maintained their unique dynamic profiles, indicating that they were not well integrated into the carbohydrate domains. The similarity in order parameters and correlation times between chitin and chitosan excluded the possibility that their signals originated from distinct polymers, instead supporting the notion of coexistence within the same polymer or as dynamically similar domains.

The cell walls of *Aspergillus* differ from those of *Rhizopus* and *Mucor* species discussed above, with a significant reduction in the chitin contribution to the rigid portion, now reinforced by a substantial presence of α-glucans and β-glucans.[32,107−109] Chemically, β-glucans have long been identified as the primary cross-linking carbohydrate, linking galactomannan and chitin.[126] However, recent ^{13}C, ^{15}N solid-state NMR studies have shown that, physically, α-glucans stack more closely with chitin to form the rigid core of the mycelial cell walls across multiple *Aspergillus* species such as *A. fumigatus* and *A. nidulans*.[35,93,108] The structural role of α-1,3-glucans, as opposed to β-1,3-glucans, in preferentially associating with chitin and supporting the rigid scaffold was confirmed through quantification of their dynamics in this study, where β-1,3-glucan exhibited smaller order parameters and faster correlation times for their motions compared to α-1,3-glucan. Long-range correlations further revealed the association between these two types of glucans within the rigid domain of *A. fumigatus* cell walls. Additionally, the number of polymorphic structures of α-1,3-glucans has now increased to five, with three forms observed in the rigid fraction of the *Aspergillus* cell walls. These forms exhibit highly comparable dynamics and correlation times, with only local structural variations. Two additional forms, induced by stress conditions, display fully rearranged helical screw conformations and are evenly distributed in both the rigid and mobile domains of the cell wall.

Unlike the filamentous fungi discussed above, the cell walls of yeast cells in *Candida* species feature a thick outer layer formed by mannan fibrils, including mannoproteins, which cover an inner layer composed of chitin, β-1,3-glucan, and β-1,6-glucan.[5,129] The ability to resolve the structure of mannan is thus crucial for studying *Candida* species. High-resolution ^1H data enabled the resolution of a large number of α-1,2-Man forms, revealing a unique structural characteristic of these large mannan fibrils. They have relatively uniform backbones but highly diverse α-1,2-linked side chains, which play a crucial role in interacting with other components to stabilize the cell wall assembly.

These new insights have enhanced our understanding of the structure and function of chitin, chitosan, glucans, and mannan in maintaining the architecture of the fungal cell walls. The availability of such capabilities has opened several new research avenues. First, it enables the exploration of the polymorphic structures of chitin and chitosan by linking them to the numerous genes encoding chitin synthases and deacetylases through the mapping of ^1H and $^{13}C/^{15}N$ chemical shifts in *chs* and *cda* mutants and treatment by inhibitors. This approach also facilitates the investigation of the polymorphic structures and biosynthetic complexity of α-glucans, such as through studies of *ags* mutants as well as mannan-based biopolymers like galactomannan, manoproteins, and mannan fibrils, which are prevalent in various fungal species.

CONCLUSIONS

In this study, we have demonstrated the power of a versatile collection of 2D/3D ^1H-detection solid-state NMR techniques for deciphering the highly polymorphic structures and heterogeneous dynamic profiles of cellular carbohydrates. The availability of different functional groups, substitutions, and distinct dynamics allowed for the clean selection of specific carbohydrate polymers within a cellular context. Partial deuteration of microbial cultures also enables the acquisition of ^1H-detection spectra with reasonable quality under moderate magnetic field strength and MAS frequencies. We also showed that site-specific dynamics of polysaccharides can be determined through relaxation measurements with the data analyzed using the simple model-free formalism. These approaches represent a significant advancement in carbohydrate structural analysis, offering unprecedented resolution and clarity for the successful identification of the carbon skeletons of polymorphic polysaccharide forms, resolving their structural variations, and mapping their spatial interactions. While demonstrated on pathogenic fungi, these techniques offer high-resolution characterization of carbohydrates across diverse organisms, enabling the mapping of acetylation patterns and the examination of amino carbohydrate distribution in intact bacterial, plant, and mammalian cells, thereby providing a deeper understanding of the structural complexity and functional diversity of crucial carbohydrates in cellular systems as well as carbohydrate-based biomaterials.

ASSOCIATED CONTENT

Supporting Information

The Supporting Information is available free of charge at https://pubs.acs.org/doi/10.1021/jacs.5c04054.

https://doi.org/10.1021/jacs.5c04054
J. Am. Chem. Soc. 2025, 147, 17416−17432

Supplementary text regarding phase cycling of the pulse sequences, relaxation rate equations, and simple model free formalism; Figures S1−S9 and Tables S1−S9 for additional NMR spectra, chemical shifts, and experimental conditions; and supplementary references (PDF)

AUTHOR INFORMATION

Corresponding Authors

Jayasubba Reddy Yarava − *Department of Chemistry, Michigan State University, East Lansing, Michigan 48824, United States;* orcid.org/0000-0002-8704-5513; Email: yaravaja@msu.edu

Tuo Wang − *Department of Chemistry, Michigan State University, East Lansing, Michigan 48824, United States;* orcid.org/0000-0002-1801-924X; Email: wangtuo1@msu.edu

Authors

Isha Gautam − *Department of Chemistry, Michigan State University, East Lansing, Michigan 48824, United States*

Anand Jacob − *Department of Chemistry, Michigan State University, East Lansing, Michigan 48824, United States*

Riqiang Fu − *National High Magnetic Field Laboratory, Florida State University, Tallahassee, Florida 32310, United States;* orcid.org/0000-0003-0075-0410

Complete contact information is available at: https://pubs.acs.org/10.1021/jacs.5c04054

Author Contributions

‡J.R.Y. and R.G. contributed equally.

Notes

The authors declare no competing financial interest.

ACKNOWLEDGMENTS

This work was supported by the National Institutes of Health (NIH) grant R01AI173270 and the National Science Foundation grant MCB-2308660. A portion of this work was performed at the National High Magnetic Field Laboratory, which is supported by National Science Foundation Cooperative Agreement No. DMR-2128556 and the State of Florida and supported in part by the National Resource for Advanced NMR Technology via NIH RM1-GM148766.

ABBREVIATIONS

AGS, α-glucan synthase; CDA, chitin deacetylase; CHS, chitin synthase; CP, cross-polarization; DIPSI-3, decoupling in the presence of scalar interactions; DQ, double-quantum; DSS, sodium trimethylsilylpropanesulfonate; EMF, extended model-free; FSLG, frequency-switched Lee−Goldburg; GAF, Gaussian axial fluctuation; GalA, galacturonic acid; GalN, galactosamine; GalNAc, *N*-acetylgalactosamine; GlcN, glucosamine; GlcNAc, *N*-acetylglucosamine; HSQC, heteronuclear single quantum coherence; INEPT, insensitive nuclei enhanced by polarization transfer; MAS, magic-angle spinning; MISSISSIPPI, multiple intense solvent suppression intended for sensitive spectroscopic investigation of protonated proteins; MurNA,c, *N*-acetylmuramic acid; NeuNAc, *N*-acetylneuraminic acid; NMR, nuclear magnetic resonance; PAR, proton-assisted recoupling; rf, radio frequency; RFDR, radio frequency-driven recoupling; slpTPPM, swept low power two-pulse phase modulation; SMF, simple model-free; SPINAL-64, small phase incremental alteration with 64 steps; TMS, tetramethylsilane; TOCSY, total correlation spectroscopy; WALTZ-16, wideband alternating-phase low-power technique for zero-residual splitting; Xyl, xylose

REFERENCES

(1) Rabinovich, G. A.; van Kooyk, Y.; Cobb, B. A. Glycobiology of Immune Responses. *Ann. N.Y. Acad. Sci.* **2012**, *1253*, 1−15.

(2) Varki, A. Biological Roles of Glycans. *Glycobiology* **2017**, *27*, 3−49.

(3) Taylor, C. M.; Roberts, I. S. Capsular Polysaccharides and Their Role in Virulence. *Concepts Bacterial Virulence* **2005**, *12*, 55−66.

(4) Cosgrove, D. J. Structure and growth of plant cell walls. *Nat. Rev. Mol. Cell Biol.* **2024**, *25*, 340−358.

(5) Gow, N. A. R.; Lenardon, M. D. Architecture of the dynamic fungal cell wall. *Nat. Rev. Microbiol.* **2023**, *21*, 248−259.

(6) Fisher, M. C.; Alastruey-Izquierdo, A.; Berman, J.; Bicanic, T.; Bignell, E. M.; Bowyer, P.; Bromley, M. J.; Bruggemann, R.; Garber, G.; Cornely, O. A.; Gurr, S. J.; Harrison, T. S.; Kuijper, E.; Rhodes, J.; Sheppard, D. C.; Warris, A.; White, P. L.; Xu, J.; Zwaan, B.; Verweij, P. E. Tackling the emerging threat of antifungal resistance to human health. *Nat. Rev. Microbiol.* **2022**, *20*, 557−571.

(7) Ghannoum, M. A.; Rice, L. B. Antifungal agents: mode of action, mechanisms of resistance, and correlation of these mechanisms with bacterial resistance. *Clin. Microbiol. Rev.* **1999**, *12*, 501−517.

(8) Bush, K.; Courvalin, P.; Dantas, G.; Davies, J.; Eisenstein, B.; Huovinen, P.; Jacoby, G. A.; Kishony, R.; Kreiswirth, B. N.; Kutter, E.; Lerner, S. A.; Levy, S.; Lewis, K.; Lomovskaya, O.; Miller, J. H.; Mobashery, S.; Piddock, L. J. V.; Projan, S.; Thomas, C. M.; Tomasz, A.; Tulkens, P. M.; Walsh, T. R.; Watson, J. D.; Witkowski, J.; Witte, W.; Wright, G.; Yeh, P.; Zgurskaya, H. I. Tackling antibiotic resistance. *Nat. Rev. Microbiol.* **2011**, *9*, 894−896.

(9) Shukla, R.; Lavore, F.; Maity, S.; Derks, M. G. N.; Jones, C. R.; Vermeulen, B. J. A.; Melcrová, A.; Morris, M. A.; Becker, L. M.; Wang, X.; Kumar, R.; Medeiros-Silva, J.; van Beekveld, R. A. M.; Bonvin, A. M. J. J.; Lorent, J. H.; Lelli, M.; Nowick, J. S.; MacGillavry, H. D.; Peoples, A. J.; Spoering, A. L.; Ling, L. L.; Hughes, D. E.; Roos, W. H.; Breukink, E.; Lewis, K.; Weingarth, M. Teixobactin kills bacteria by a two-pronged attack on the cell envelope. *Nature* **2022**, *608*, 390−396.

(10) Weis, W. I.; Drickamer, K. Structural Basis of Lectin-Carbohydrate Recogonition. *Annu. Rev. Biochem.* **1996**, *65*, 441−473.

(11) Dwek, R. A. Glycobiology: Toward Understanding the Function of Sugars. *Chem. Rev.* **1996**, *96*, 683−720.

(12) Zhao, W.; Deligey, F.; Shekar, S. C.; Mentink-Vigier, F.; Wang, T. Current limitations of solid-state NMR in carbohydrate and cell wall research. *J. Magn. Reson.* **2022**, *341*, No. 107263.

(13) Duus, J.; Gotfredsen, C. H.; Bock, K. Carbohydrate Structural Determination by NMR Spectroscopy: Modern Methods and Limitations. *Chem. Rev.* **2000**, *100*, 4589−4614.

(14) Chow, W. Y.; De Paëpe, G.; Hediger, S. Biomolecular and Biological Applications of Solid-State NMR with Dynamic Nuclear Polarization Enhancement. *Chem. Rev.* **2022**, *122*, 9795−9847.

(15) Ghassemi, N.; Poulhazan, A.; Deligey, F.; Mentink-Vigier, F.; Marcotte, I.; Wang, T. Solid-State NMR Investigations of Extracellular Matrixes and Cell Walls of Algae, Bacteria, Fungi, and Plants. *Chem. Rev.* **2022**, *122*, 10036−10086.

(16) Reif, B.; Ashbrook, S. E.; Emsley, L.; Hong, M. Solid-State NMR Spectroscopy. *Nat. Rev. Methods Primers* **2021**, *1*, 2.

(17) Kern, T.; Giffard, M.; Hediger, S.; Amoroso, A.; Giustini, C.; Bui, N. K.; Joris, B.; Bougault, C.; Vollmer, W.; Simorre, J.-P. Dynamics characterization of fully hydrated bacterial cell walls by solid-state NMR: evidence for cooperative binding of metal ions. *J. Am. Chem. Soc.* **2010**, *132*, 10911−10919.

(18) Romaniuk, J. A. H.; Cegelski, L. Bacterial cell wall composition and the influence of antibiotics by cell-wall and whole-cell NMR. *Philos. Trans. R. Soc., B* **2015**, *370*, No. 20150024.

(19) Xue, Y.; Yu, C.; Ouyang, H.; Huang, J.; Kang, X. Uncovering the Molecular Composition and Architecture of the Bacillus subtilis Biofilm via Solid-State NMR Spectroscopy. *J. Am. Chem. Soc.* **2024**, *146*, 11906−11923.

(20) Byeon, C. H.; Kinney, T.; Saricayir, H.; Hansen, K. H.; Scott, F. J.; Sirinivasa, S.; Wells, M. K.; Mentink-Vigier, F.; Kim, W.; Akbey, Ü. Ultrasensitive Characterization of Native Bacterial Biofilms via Dynamic Nuclear Polarization-Enhanced Solid-State NMR. *Angew. Chem., Int. Ed.* **2025**, *64*, No. e202418146.
(21) Reichhardt, C.; Cegelski, L. Solid-State NMR for Bacterial Biofilms. *Mol. Phys.* **2014**, *112*, 887−894.
(22) Temple, H.; Phyo, P.; Yang, W.; Lyczakowski, J. J.; Echevarria-Poza, A.; Yakunin, I.; Parra-Rojas, J. P.; Terrett, O. M.; Saez-Aguayo, S.; Dupree, R.; Orellana, A.; Hong, M.; Dupree, P. Golgi-localized putative S-adenosyl methionine transporters required for plant cell wall polysaccharide methylation. *Nat. Plants* **2022**, *8*, 656−669.
(23) Kirui, A.; Du, J.; Zhao, W.; Barnes, W.; Kang, X.; Anderson, C. T.; Xiao, C.; Wang, T. A pectin methyltransferase modulates polysaccharide dynamics and interactions in Arabidopsis primary cell walls: evidence from solid-state NMR. *Carbohydr. Polym.* **2021**, *270*, No. 118370.
(24) Perez Garcia, M.; Zhang, Y.; Hayes, J.; Salazar, A.; Zabotina, O. A.; Hong, M. Structure and interactions of plant cell-wall polysaccharides by two-and three-dimensional magic-angle-spinning solid-state NMR. *Biochemistry* **2011**, *50*, 989−1000.
(25) Simmons, T. J.; Mortimer, J. C.; Bernardinelli, O. D.; Poppler, A. C.; Brown, S. P.; deAzevedo, E. R.; Dupree, R.; Dupree, P. Folding of xylan onto cellulose fibrils in plant cell walls revealed by solid-state NMR. *Nat. Commun.* **2016**, *7*, 13902.
(26) Duan, P.; Kaser, S.; Lyczakowski, J. J.; Phyo, P.; Tryfona, T.; Dupree, P.; Hong, M. Xylan Structure and Dynamics in Native Brachypodium Grass Cell Walls Investigated by Solid-State NMR Spectroscopy. *ACS Omega* **2021**, *6*, 15460−15471.
(27) Kirui, A.; Zhao, W.; Deligey, F.; Yang, H.; Kang, X.; Mentink-Vigier, F.; Wang, T. Carbohydrate-aromatic interface and molecular architecture of lignocellulose. *Nat. Commun.* **2022**, *13*, 538.
(28) Kang, X.; Kirui, A.; Dickwella Widanage, M. C.; Mentink-Vigier, F.; Cosgrove, D. J.; Wang, T. Lignin-polysaccharide interactions in plant secondary cell walls revealed by solid-state NMR. *Nat. Commun.* **2019**, *10*, 347.
(29) Terrett, O. M.; Lyczakowski, J. J.; Yu, L.; Iuga, D.; Franks, W. T.; Brown, S. P.; Dupree, R.; Dupree, P. Molecular architecture of softwood revealed by solid-state NMR. *Nat. Commun.* **2019**, *10*, 4978.
(30) Chatterjee, S.; Prados-Rosales, R.; Itin, B.; Casadevall, A.; Stark, R. E. Solid-state NMR Reveals the Carbon-based Molecular Architecture of Cryptococcus neoformans Fungal Eumelanins in the Cell Wall. *J. Biol. Chem.* **2015**, *290*, 13779−13790.
(31) Ehren, H. L.; Appels, F. V. W.; Houben, K.; Renault, M. A. M.; Wosten, H. A. B.; Baldus, M. Characterization of the cell wall of a mushroom forming fungus at atomic resolution using solid-state NMR spectroscopy. *Cell Surf.* **2020**, *6*, No. 100046.
(32) Lamon, G.; Lends, A.; Valsecchi, I.; Wong, S. S. W.; Duprès, V.; Lafont, F.; Tolchard, J.; Schmitt, C.; Mallet, A.; Grélard, A.; Morvan, E.; Dufourc, E. J.; Habenstein, B.; Guijarro, J. I.; Aimanianda, V.; Loquet, A. Solid-state NMR molecular snapshots of Aspergillus fumigatus cell wall architecture during a conidial morphotype transition. *Proc. Natl. Acad. Sci. U. S. A.* **2023**, *120*, No. e2212003120.
(33) Lends, A.; Lamon, G.; Delcourte, L.; Surny-Leclere, A.; Grelard, A.; Morvan, E.; Abdul-Shukkoor, M. B.; Berbon, M.; Vallet, A.; Habenstein, B.; Dufourc, E. J.; Schanda, P.; Aimanianda, V.; Loquet, A. Molecular Distinction of Cell Wall and Capsular Polysaccharides in Encapsulated Pathogens by In Situ Magic-Angle Spinning NMR Techniques. *J. Am. Chem. Soc.* **2025**, *147*, 6813−6824.
(34) Safeer, A.; Kleijburg, F.; Bahri, S.; Beriashvili, D.; Veldhuizen, E. J. A.; van Neer, J.; Tegelaar, M.; de Cock, H.; Wösten, H. A. B.; Baldus, M. Probing Cell-Surface Interactions in Fungal Cell Walls by High-Resolution 1H-Detected Solid-State NMR Spectroscopy. *Chem. - Eur. J.* **2023**, *29*, No. e202202616.
(35) Kang, X.; Kirui, A.; Muszynski, A.; Widanage, M. C. D.; Chen, A.; Azadi, P.; Wang, P.; Mentink-Vigier, F.; Wang, T. Molecular architecture of fungal cell walls revealed by solid-state NMR. *Nat. Commun.* **2018**, *9*, 2747.
(36) Le Marchand, T.; Schubeis, T.; Bonaccorsi, M.; Paluch, P.; Lalli, D.; Pell, A. J.; Andreas, L. B.; Jaudzems, K.; Stanek, J.; Pintacuda, G. 1H-Detected Biomolecular NMR under Fast Magic-Angle Spinning. *Chem. Rev.* **2022**, *122*, 9943−10018.
(37) Su, Y.; Andreas, L. B.; Griffin, R. G. Magic Angle Spinning NMR of Proteins: High-Frequency Dynamic Nuclear Polarization and 1H Detection. *Annu. Rev. Biochem.* **2015**, *84*, 465−497.
(38) Zhou, D. H.; Shah, G.; Cormos, M.; Mullen, C.; Sandoz, D.; Rienstra, C. M. Proton-Detected Solid-State NMR Spectroscopy of Fully Protonated Proteins at 40 kHz Magic-Angle Spinning. *J. Am. Chem. Soc.* **2007**, *129*, 11791−11801.
(39) Andreas, L. B.; Jaudzems, K.; Stanek, J.; Lalli, D.; Bertarello, A.; Le Marchand, T.; Cala-De Paepe, D.; Kotelovica, S.; Akopjana, I.; Knott, B.; Wegner, S.; Engelke, F.; Lesage, A.; Emsley, L.; Tars, K.; Herrmann, T.; Pintacuda, G. Structure of fully protonated proteins by proton-detected magic-angle spinning NMR. *Proc. Natl. Acad. Sci. U.S.A.* **2016**, *113*, 9187−9192.
(40) McDermott, A. E.; Creuzet, F. J.; Kolbert, A. C.; Griffin, R. G. High-resolution magic-angle-spinning NMR spectra of protons in deuterated solids. *J. Magn. Reson.* **1992**, *98*, 408−413.
(41) Chevelkov, V.; Rehbein, K.; Diehl, A.; Reif, B. Ultrahigh Resolution in Proton Solid-State NMR Spectroscopy at High Levels of Deuteration. *Angew. Chem., Int. Ed.* **2006**, *45*, 3878−3881.
(42) Callon, M.; Luder, D.; Malär, A. A.; Wiegand, T.; Ř́mal, V.; Lecoq, L.; Böckmann, A.; Samoson, A.; Meier, B. H. High and fast: NMR protein−proton side-chain assignments at 160 kHz and 1.2 GHz. *Chem. Sci.* **2023**, *14*, 10824−10834.
(43) Schwalbe, H. Editorial: New 1.2 GHz NMR Spectrometers—New Horizons? *Angew. Chem., Int. Ed.* **2017**, *56*, 10252−10253.
(44) Barbet-Massin, E.; Pell, A. J.; Retel, J. S.; Andreas, L. B.; Jaudzems, K.; Franks, W. T.; Nieuwkoop, A. J.; Hiller, M.; Higman, V.; Guerry, P.; Bertarello, A.; Knight, M. J.; Felletti, M.; Le Marchand, T.; Kotelovica, S.; Akopjana, I.; Tars, K.; Stoppini, M.; Bellotti, V.; Bolognesi, M.; Ricagno, S.; Chou, J. J.; Griffin, R. G.; Oschkinat, H.; Lesage, A.; Emsley, L.; Herrmann, T.; Pintacuda, G. Rapid Proton-Detected NMR Assignment for Proteins with Fast Magic Angle Spinning. *J. Am. Chem. Soc.* **2014**, *136*, 12489−12497.
(45) Agarwal, V.; Diehl, A.; Skrynnikov, N.; Reif, B. High Resolution ^{1}H Detected ^{1}H,^{13}C Correlation Spectra in MAS Solid-State NMR using Deuterated Proteins with Selective ^{1}H,^{2}H Isotopic Labeling of Methyl Groups. *J. Am. Chem. Soc.* **2006**, *128*, 12620−12621.
(46) Ahlawat, S.; Mote, K. R.; Lakomek, N.-A.; Agarwal, V. Solid-State NMR: Methods for Biological Solids. *Chem. Rev.* **2022**, *122*, 9643−9737.
(47) Nishiyama, Y.; Hou, G.; Agarwal, V.; Su, Y.; Ramamoorthy, A. Ultrafast Magic Angle Spinning Solid-State NMR Spectroscopy: Advances in Methodology and Applications. *Chem. Rev.* **2023**, *123*, 918−988.
(48) Samoson, A. H-MAS. *J. Magn. Reson.* **2019**, *306*, 167−172.
(49) Yuan, E. C.-Y.; Huang, S.-J.; Huang, H.-C.; Sinkkonen, J.; Oss, A.; Org, M.-L.; Samoson, A.; Tai, H.-C.; Chan, J. C. C. Faster magic angle spinning reveals cellulose conformations in woods. *Chem. Commun.* **2021**, *57*, 4110−4113.
(50) Zhang, Z.; Oss, A.; Org, M. L.; Samoson, A.; Li, M.; Tan, H.; Su, Y.; Yang, J. Selectively Enhanced 1H−1H Correlations in Proton-Detected Solid-State NMR under Ultrafast MAS Conditions. *J. Phys. Chem. Lett.* **2020**, *11*, 8077−8083.
(51) Akbey, Ü.; Lange, S.; Trent Franks, W.; Linser, R.; Rehbein, K.; Diehl, A.; van Rossum, B.-J.; Reif, B.; Oschkinat, H. Optimum levels of exchangeable protons in perdeuterated proteins for proton detection in MAS solid-state NMR spectroscopy. *J. Biomol. NMR* **2010**, *46*, 67−73.
(52) Agarwal, V.; Reif, B. Residual methyl protonation in perdeuterated proteins for multi-dimensional correlation experiments in MAS solid-state NMR spectroscopy. *J. Magn. Reson.* **2008**, *194*, 16−24.
(53) Asami, S.; Schmieder, P.; Reif, B. High Resolution 1H-Detected Solid-State NMR Spectroscopy of Protein Aliphatic Resonances: Access to Tertiary Structure Information. *J. Am. Chem. Soc.* **2010**, *132*, 15133−15135.

https://doi.org/10.1021/jacs.5c04054
J. Am. Chem. Soc. 2025, 147, 17416−17432

(54) Nand, D.; Cukkemane, A.; Becker, S.; Baldus, M. Fractional deuteration applied to biomolecular solid-state NMR spectroscopy. *J. Biomol. NMR* **2012**, *52*, 91−101.
(55) Cala-De Paepe, D.; Stanek, J.; Jaudzems, K.; Tars, K.; Andreas, L. B.; Pintacuda, G. Is protein deuteration beneficial for proton detected solid-state NMR at and above 100 kHz magic-angle spinning? *ssNMR* **2017**, *87*, 126−136.
(56) Zhou, D. H.; Shea, J. J.; Nieuwkoop, A. J.; Franks, W. T.; Wylie, B. J.; Mullen, C.; Sandoz, D.; Rienstra, C. M. Solid-State Protein-Structure Determination with Proton-Detected Triple-Resonance 3D Magic-Angle-Spinning NMR Spectroscopy. *Angew. Chem., Int. Ed.* **2007**, *46*, 8380−8383.
(57) Siemer, A. B. Advances in studying protein disorder with solid-state NMR. *Solid State Nucl. Magn. Reson.* **2020**, *106*, No. 101643.
(58) Retel, J. S.; Nieuwkoop, A. J.; Hiller, M.; Higman, V. A.; Barbet-Massin, E.; Stanek, J.; Andreas, L. B.; Franks, W. T.; van Rossum, B. J.; Vinothkumar, K. R.; Handel, L.; de Palma, G. G.; Bardiaux, B.; Pintacuda, G.; Emsley, L.; Kühlbrandt, W.; Oschkinat, H. Structure of outer membrane protein G in lipid bilayers. *Nat. Commun.* **2017**, *8*, 2073.
(59) Marchanka, A.; Stanek, J.; Pintacuda, G.; Carlomagno, T. Rapid access to RNA resonances by proton-detected solid-state NMR at > 100 kHz MAS. *Chem. Commun.* **2018**, *54*, 8972−8975.
(60) Struppe, J.; Quinn, C. M.; Lu, M.; Wang, M.; Hou, G.; Lu, X.; Kraus, J.; Andreas, L. B.; Stanek, J.; Lalli, D.; Lesage, A.; Pintacuda, G.; Maas, W.; Gronenborn, A. M.; Polenova, T. Expanding the horizons for structural analysis of fully protonated protein assemblies by NMR spectroscopy at MAS frequencies above 100 kHz. *Solid State Nucl. Magn. Reson.* **2017**, *87*, 117−125.
(61) Sarkar, S.; Runge, B.; Russell, R. W.; Movellan, K. T.; Calero, D.; Zeinalilathori, S.; Quinn, C. M.; Lu, M.; Calero, G.; Gronenborn, A. M.; Polenova, T. Atomic-Resolution Structure of SARS-CoV-2 Nucleocapsid Protein N-Terminal Domain. *J. Am. Chem. Soc.* **2022**, *144*, 10543−10555.
(62) Roske, Y.; Lindemann, F.; Diehl, A.; Cremer, N.; Higman, V. A.; Schlegel, B.; Leidert, M.; Driller, K.; Turgay, K.; Schmieder, P.; Heinemann, U.; Oschkinat, H. TapA acts as specific chaperone in TasA filament formation by strand complementation. *Proc. Natl. Acad. Sci. U. S. A.* **2023**, *120*, No. e2217070120.
(63) Wälti, M. A.; Ravotti, F.; Arai, H.; Glabe, C. G.; Wall, J. S.; Böckmann, A.; Güntert, P.; Meier, B. H.; Riek, R. Atomic-resolution structure of a disease-relevant Aβ(1−42) amyloid fibril. *Proc. Natl. Acad. Sci. U. S. A.* **2016**, *113* (34), E4976−E4984.
(64) Colvin, M. T.; Silvers, R.; Frohm, B.; Su, Y.; Linse, S.; Griffin, R. G. High Resolution Structural Characterization of Aβ42 Amyloid Fibrils by Magic Angle Spinning NMR. *J. Am. Chem. Soc.* **2015**, *137*, 7509−7518.
(65) Maruyoshi, K.; Iuga, D.; Antzutkin, O. N.; Alhalaweh, A.; Velaga, S. P.; Brown, S. P. Identifying the intermolecular hydrogen-bonding supramolecular synthons in an indomethacin−nicotinamide cocrystal by solid-state NMR. *Chem. Commun.* **2012**, *48*, 10844−10846.
(66) Wijesekara, A. V.; Venkatesh, A.; Lampkin, B. J.; VanVeller, B.; Lubach, J. W.; Nagapudi, K.; Hung, I.; Gor'kov, P. L.; Gan, Z.; Rossini, A. J. Fast Acquisition of Proton-Detected HETCOR Solid-State NMR Spectra of Quadrupolar Nuclei and Rapid Measurement of NH Bond Lengths by Frequency Selective HMQC and RESPDOR Pulse Sequences. *Chem. - Eur. J.* **2020**, *26*, 7881−7888.
(67) Brown, S. P. Applications of high-resolution 1H solid-state NMR. *Solid State Nucl. Magn. Reson.* **2012**, *41*, 1−27.
(68) Damron, J. T.; Kersten, K. M.; Pandey, M. K.; Mroue, K. H.; Yarava, J. R.; Nishiyama, Y.; Matzger, A. J.; Ramamoorthy, A. Electrostatic Constraints Assessed by ^{1}H MAS NMR Illuminate Differences in Crystalline Polymorphs. *J. Phys. Chem. Lett.* **2017**, *8*, 4253−4257.
(69) Hirsh, D. A.; Wijesekara, A. V.; Carnahan, S. L.; Hung, I.; Lubach, J. W.; Nagapudi, K.; Rossini, A. J. Rapid Characterization of Formulated Pharmaceuticals Using Fast MAS ^{1}H Solid-State NMR Spectroscopy. *Mol. Pharmaceutics* **2019**, *16*, 3121−3132.
(70) Cordova, M.; Moutzouri, P.; Simões de Almeida, B.; Torodii, D.; Emsley, L. Pure Isotropic Proton NMR Spectra in Solids using Deep Learning. *Angew. Chem., Int. Ed.* **2023**, *62*, No. e202216607.
(71) Lewandowski, J. R.; Sass, H. J.; Grzesiek, S.; Blackledge, M.; Emsley, L. Site-Specific Measurement of Slow Motions in Proteins. *J. Am. Chem. Soc.* **2011**, *133*, 16762−16765.
(72) Lakomek, N.-A.; Penzel, S.; Lends, A.; Cadalbert, R.; Ernst, M.; Meier, B. H. Microsecond Dynamics in Ubiquitin Probed by Solid-State 15N NMR Spectroscopy R1ρ Relaxation Experiments under Fast MAS (60−110 kHz). *Chem. - Eur. J.* **2017**, *23*, 9425−9433.
(73) Schanda, P.; Ernst, M. Studying dynamics by magic-angle spinning solid-state NMR spectroscopy: Principles and applications to biomolecules. *Prog. Nucl. Magn. Reson. Spectrosc.* **2016**, *96*, 1−46.
(74) Busi, B.; Yarava, J. R.; Bertarello, A.; Freymond, F.; Adamski, W.; Maurin, D.; Hiller, M.; Oschkinat, H.; Blackledge, M.; Emsley, L. Similarities and Differences among Protein Dynamics Studied by Variable Temperature Nuclear Magnetic Resonance Relaxation. *J. Phys. Chem. B* **2021**, *125*, 2212−2221.
(75) Haller, J. D.; Schanda, P. Amplitudes and time scales of picosecond-to-microsecond motion in proteins studied by solid-state NMR: a critical evaluation of experimental approaches and application to crystalline ubiquitin. *J. Biomol. NMR* **2013**, *57*, 263−280.
(76) Kurauskas, V.; Izmailov, S. A.; Rogacheva, O. N.; Hessel, A.; Ayala, I.; Woodhouse, J.; Shilova, A.; Xue, Y.; Yuwen, T.; Coquelle, N.; Colletier, J.-P.; Skrynnikov, N. R.; Schanda, P. Slow conformational exchange and overall rocking motion in ubiquitin protein crystals. *Nat. Commun.* **2017**, *8*, 145.
(77) Öster, C.; Kosol, S.; Lewandowski, J. R. Quantifying Microsecond Exchange in Large Protein Complexes with Accelerated Relaxation Dispersion Experiments in the Solid State. *Sci. Rep.* **2019**, *9*, 11082.
(78) Lipari, G.; Szabo, A. Model-free approach to the interpretation of nuclear magnetic resonance relaxation in macromolecules. 2. Analysis of experimental results. *J. Am. Chem. Soc.* **1982**, *104*, 4559−4570.
(79) Lewandowski, J. R.; Sein, J.; Blackledge, M.; Emsley, L. Anisotropic Collective Motion Contributes to Nuclear Spin Relaxation in Crystalline Proteins. *J. Am. Chem. Soc.* **2010**, *132*, 1246−1248.
(80) Giraud, N.; Blackledge, M.; Goldman, M.; Böckmann, A.; Lesage, A.; Penin, F.; Emsley, L. Quantitative Analysis of Backbone Dynamics in a Crystalline Protein from Nitrogen-15 Spin−Lattice Relaxation. *J. Am. Chem. Soc.* **2005**, *127*, 18190−18201.
(81) Saurel, O.; Iordanov, I.; Nars, G.; Demange, P.; Le Marchand, T.; Andreas, L. B.; Pintacuda, G.; Milon, A. Local and Global Dynamics in Klebsiella pneumoniae Outer Membrane Protein a in Lipid Bilayers Probed at Atomic Resolution. *J. Am. Chem. Soc.* **2017**, *139*, 1590−1597.
(82) Good, D.; Pham, C.; Jagas, J.; Lewandowski, J. R.; Ladizhansky, V. Solid-State NMR Provides Evidence for Small-Amplitude Slow Domain Motions in a Multispanning Transmembrane α-Helical Protein. *J. Am. Chem. Soc.* **2017**, *139*, 9246−9258.
(83) Smith, A. A.; Ernst, M.; Meier, B. H. Optimized "detectors" for dynamics analysis in solid-state NMR. *J. Chem. Phys.* **2018**, *148*, No. 045104.
(84) Smith, A. A.; Ernst, M.; Riniker, S.; Meier, B. H. Localized and Collective Motions in HET-s(218−289) Fibrils from Combined NMR Relaxation and MD Simulation. *Angew. Chem., Int. Ed.* **2019**, *58*, 9383−9388.
(85) Schanda, P.; Meier, B. H.; Ernst, M. Accurate measurement of one-bond H−X heteronuclear dipolar couplings in MAS solid-state NMR. *J. Magn. Reson.* **2011**, *210*, 246−259.
(86) Paluch, P.; Trébosc, J.; Nishiyama, Y.; Potrzebowski, M. J.; Malon, M.; Amoureux, J. P. Theoretical study of CP-VC: A simple, robust and accurate MAS NMR method for analysis of dipolar C−H interactions under rotation speeds faster than ca. 60kHz. *J. Magn. Reson.* **2015**, *252*, 67−77.
(87) Taware, P. P.; Jain, M. G.; Raran-Kurussi, S.; Agarwal, V.; Madhu, P. K.; Mote, K. R. Measuring Dipolar Order Parameters in Nondeuterated Proteins Using Solid-State NMR at the Magic-Angle-Spinning Frequency of 100 kHz. *J. Phys. Chem. Lett.* **2023**, *14*, 3627−3635.

(88) Duan, P.; Hong, M. Selective Detection of Intermediate-Amplitude Motion by Solid-State NMR. *J. Phys. Chem. B* **2024**, *128*, 2293−2303.
(89) Phyo, P.; Hong, M. Fast MAS $^{1}H-^{13}C$ correlation NMR for structural investigations of plant cell walls. *J. Biomol. NMR* **2019**, *73*, 661−674.
(90) Bahri, S.; Safeer, A.; Adler, A.; Smedes, H.; van Ingen, H.; Baldus, M. 1H-detected characterization of carbon−carbon networks in highly flexible protonated biomolecules using MAS NMR. *J. Biomol. NMR* **2023**, *77*, 111−119.
(91) Bougault, C.; Ayala, I.; Vollmer, W.; Simorre, J.-P.; Schanda, P. Studying intact bacterial peptidoglycan by proton-detected NMR spectroscopy at 100 kHz MAS frequency. *J. Struct. Biol.* **2019**, *206*, 66−72.
(92) Vallet, A.; Ayala, I.; Perrone, B.; Hassan, A.; Simorre, J. P.; Bougault, C.; Schanda, P. MAS NMR experiments of corynebacterial cell walls: Complementary ^{1}H- and CPMAS CryoProbe-enhanced 13C-detected experiments. *J. Magn. Reson.* **2024**, *364*, No. 107708.
(93) Gautam, I.; Yarava, J. R.; Xu, Y.; Li, R.; Scott, F. J.; Mentink-Vigier, F.; Momany, M.; Latgé, J.-P.; Wang, T. Comparative analysis of polysaccharide and cell wall structure in Aspergillus nidulans and Aspergillus fumigatus by solid-state NMR. *Carbohydr. Polym.* **2025**, *348*, No. 122907.
(94) Cheng, Q.; Dickwella Widanage, M. C.; Yarava, J. R.; Ankur, A.; Latgé, J.-P.; Wang, P.; Wang, T. Molecular architecture of chitin and chitosan-dominated cell walls in zygomycetous fungal pathogens by solid-state NMR. *Nat. Commun.* **2024**, *15*, 8295.
(95) Dickwella Widanage, M. C.; Singh, K.; Li, J.; Yarava, J. R.; Scott, F. J.; Xu, Y.; Gow, N. A. R.; Mentink-Vigier, F.; Wang, P.; Lamoth, F.; Wang, T. Unveiling Cell Wall Structure and Echinocandin Response in Candida auris and Candida albicans via Solid-State NMR. *bioRxiv* **2024**, DOI: .
(96) Brown, G. D.; Denning, D. W.; Gow, N. A. R.; Levitz, S. M.; Netea, M. G.; White, T. C. Hidden killers: human fungal infections. *Sci. Transl. Med.* **2012**, *4*, 165rv13.
(97) Latgé, J. P.; Chamilos, G. Aspergillus fumigatus and Aspergillosis in 2019. *Clin. Microbiol. Rev.* **2019**, *33*, No. e0014018.
(98) Katsipoulaki, M.; Stappers, M. H. T.; Malavia-Jones, D.; Brunke, S.; Hube, B.; Gow, N. A. R. Candida albicans and Candida glabrata: global priority pathogens. *Microbiol. Mol. Biol. Rev.* **2024**, *88*, No. e0002123.
(99) Hoenigl, M.; Seidel, D.; Sprute, R.; Cunha, C.; Oliverio, M.; Goldman, G. H.; Ibrahim, A. S.; Carvalho, A. COVID-19-associated fungal infections. *Nat. Microbiol.* **2022**, *7*, 1127−1140.
(100) Fiebig, T.; Cramer, J. T.; Bethe, A.; Baruch, P.; Curth, U.; Führing, J. I.; Buettner, F. F. R.; Vogel, U.; Schubert, M.; Fedorov, R.; Mühlenhoff, M. Structural and mechanistic basis of capsule O-acetylation in Neisseria meningitidis serogroup A. *Nat. Commun.* **2020**, *11*, 4723.
(101) Li, H.; Wang, Y.; Zhao, P.; Guo, L.; Huang, L.; Li, X.; Gao, W. Naturally and chemically acetylated polysaccharides: Structural characteristics, synthesis, activities, and applications in the delivery system: A review. *Carbohydr. Polym.* **2023**, *313*, No. 120746.
(102) Chen, X.; Varki, A. Advances in the Biology and Chemistry of Sialic Acids. *ACS Chem. Biol.* **2010**, *5*, 163−176.
(103) Reily, C.; Stewart, T. J.; Renfrow, M. B.; Novak, J. Glycosylation in health and disease. *Nat. Rev. Nephrol.* **2019**, *15*, 346−366.
(104) El Nokab, M. E. H.; van der Wel, P. C. A. Use of Solid-state NMR spectroscopy for Investigating Polysaccharide-based Hydrogels: A Review. *Carbohydr. Polym.* **2020**, *240*, No. 116276.
(105) Rampratap, P.; Lasorsa, A.; Perrone, B.; van der Wel, P. C. A.; Walvoort, M. T. C. Production of isotopically enriched high molecular weight hyaluronic acid and characterization by solid-state NMR. *Carbohydr. Polym.* **2023**, *316*, No. 121063.
(106) Poulhazan, A.; Arnold, A. A.; Mentink-Vigier, F.; Muszyński, A.; Azadi, P.; Halim, A.; Vakhrushev, S. Y.; Joshi, H. J.; Wang, T.; Warschawski, D. E.; Marcotte, I. Molecular-level architecture of Chlamydomonas reinhardtii's glycoprotein-rich cell wall. *Nat. Commun.* **2024**, *15*, 986.
(107) Dickwella Widanage, M. C.; Gautam, I.; Sarkar, D.; Mentink-Vigier, F.; Vermass, J. V.; Ding, S. Y.; Lipton, A. S.; Fontaine, T.; Latgé, J. P.; Wang, P.; Wang, T. Adaptative survival of Aspergillus fumigatus to echinocandins arises from cell wall remodeling beyond β−1,3-glucan synthesis inhibition. *Nat. Commun.* **2024**, *15*, 6382.
(108) Fernando, L. D.; Pérez-Llano, Y.; Dickwella Widanage, M. C.; Jacob, A.; Martínez-Ávila, L.; Lipton, A. S.; Gunde-Cimerman, N.; Latgé, J. P.; Batista-García, R. A.; Wang, T. Structural adaptation of fungal cell wall in hypersaline environment. *Nat. Commun.* **2023**, *14*, 7082.
(109) Chakraborty, A.; Fernando, L. D.; Fang, W.; Dickwella Widanage, M. C.; Wei, P.; Jin, C.; Fontaine, T.; Latgé, J. P.; Wang, T. A molecular vision of fungal cell wall organization by functional genomics and solid-state NMR. *Nat. Commun.* **2021**, *12*, 6346.
(110) Nishiyama, Y.; Zhang, R.; Ramamoorthy, A. Finite-pulse radio frequency driven recoupling with phase cycling for 2D $^{1}H/^{1}H$ correlation at ultrafast MAS frequencies. *J. Magn. Reson.* **2014**, *243*, 25−32.
(111) Bennett, A. E.; Rienstra, C. M.; Griffiths, J. M.; Zhen, W.; Lansbury, P. T.; Griffin, R. G. Homonuclear radio frequency-driven recoupling in rotating solids. *J. Chem. Phys.* **1998**, *108*, 9463−9479.
(112) Shaka, A.; Keeler, J.; Frenkiel, T.; Freeman, R. An improved sequence for broadband decoupling: WALTZ-16. *J. Magn. Reson.* **1983**, *52*, 335−338.
(113) Bodenhausen, G.; Ruben, D. J. Natural abundance nitrogen-15 NMR by enhanced heteronuclear spectroscopy. *Chem. Phys. Lett.* **1980**, *69*, 185−189.
(114) Burum, D. P. HETCOR in Organic Solids. In *eMagRes*; Harris, R. K.; Wasylishen, R., Eds. John Wiley & Sons, Ltd: Chichester, UK, 2007; pp 1−6.
(115) Lewandowski, J. R.; Sein, J.; Sass, H. J.; Grzesiek, S.; Blackledge, M.; Emsley, L. Measurement of Site-Specific ^{13}C Spin−Lattice Relaxation in a Crystalline Protein. *J. Am. Chem. Soc.* **2010**, *132*, 8252−8254.
(116) Fung, B. M.; Khitrin, A. K.; Ermolaev, K. An Improved Broadband Decoupling Sequence for Liquid Crystals and Solids. *J. Magn. reson.* **2000**, *142*, 97−101.
(117) Zhou, D. H.; Rienstra, C. M. High-performance solvent suppression for proton detected solid-state NMR. *J. Magn. Reson.* **2008**, *192*, 167−172.
(118) Marion, D.; Ikura, M.; Tschudin, R.; Bax, A. Rapid recording of 2D NMR spectra without phase cycling. Application to the study of hydrogen exchange in proteins. *J. Magn. Reson.* **1989**, *85*, 393−399.
(119) Vollmer, W.; Blanot, D.; De Pedro, M. A. Peptidoglycan structure and architecture. *FEMS Microbiol. Rev.* **2008**, *32*, 149−167.
(120) Delcourte, L.; Berbon, M.; Rodriguez, M.; Delhaes, L.; Habenstein, B.; Loquet, A. Solid-state NMR observation of chitin in whole cells by indirect ^{15}N detection with NC, NCC, CNC and CNCC polarization transfers. *Solid State Nucl. Magn. Reson.* **2025**, *137*, No. 102002.
(121) Fernando, L. D.; Dickwella Widanage, M. C.; Penfield, J.; Lipton, A. S.; Washton, N.; Latgé, J. P.; Wang, P.; Zhang, L.; Wang, T. Structural polymorphism of chitin and chitosan in fungal cell walls from solid-state NMR and principal component analysis. *Front. Mol. Biosci.* **2021**, *8*, No. 727053.
(122) Shahin, L.; Zhang, L.; Mohnen, D.; Urbanowicz, B. R. Insights into pectin O-acetylation in the plant cell wall: structure, synthesis, and modification. *Cell Surf.* **2023**, *9*, No. 100099.
(123) Reith, J.; Mayer, C. Characterization of a Glucosamine/Glucosaminide N-Acetyltransferase of Clostridium acetobutylicum. *J. Bacteriol.* **2011**, *193*, 5393−5399.
(124) Stanek, J.; Andreas, L. B.; Jaudzems, K.; Cala, D.; Lalli, D.; Bertarello, A.; Schubeis, T.; Akopjana, I.; Kotelovica, S.; Tars, K.; Pica, A.; Leone, S.; Picone, D.; Xu, Z.-Q.; Dixon, N. E.; Martinez, D.; Berbon, M.; El Mammeri, N.; Noubhani, A.; Saupe, S.; Habenstein, B.; Loquet, A.; Pintacuda, G. NMR Spectroscopic Assignment of Backbone and Side-Chain Protons in Fully Protonated Proteins: Microcrystals, Sedimented Assemblies, and Amyloid Fibrils. *Angew. Chem., Int. Ed.* **2016**, *55*, 15504−15509.

(125) Chevelkov, V.; Van Rossum, B. J.; Castellani, F.; Rehbein, K.; Diehl, A.; Hohwy, M.; Steuernagel, S.; Engelke, F.; Oschkinat, H.; Reif, B. ^{1}H detection in MAS solid-state NMR spectroscopy of biomacromolecules employing pulsed field gradients for residual solvent suppression. *J. Am. Chem. Soc.* **2003**, *125*, 7788−7789.
(126) Gastebois, A.; Clavaud, C.; Aimanianda, V.; Latgé, J.-P. Aspergillus fumigatus: cell wall polysaccharides, their biosynthesis and organization. *Future Microbiol.* **2009**, *4*, 583−595.
(127) Fontaine, T.; Beauvais, A.; Loussert, C.; Thevenard, B.; Fulgsang, C. C.; Ohno, N.; Clavaud, C.; Prevost, M. C.; Latgé, J. P. Cell wall alpha1−3glucans induce the aggregation of germinating conidia of Aspergillus fumigatus. *Fungal Genet. Biol.* **2010**, *47*, 707−712.
(128) Latgé, J. P.; Wang, T. Modern Biophysics Redefines Our Understanding of Fungal Cell Wall Structure, Complexity, and Dynamics. *mBio* **2022**, *13*, No. e0114522.
(129) Lenardon, M. D.; Sood, P.; Dorfmueller, H. C.; Brown, A. J. P.; Gow, N. A. R. Scalar nanostructure of the Candida albicans cell wall; a molecular, cellular and ultrastructural analysis and interpretation. *Cell Surf.* **2020**, *6*, No. 100047.
(130) Lamley, J. M.; Lougher, M. J.; Sass, H. J.; Rogowski, M.; Grzesike, S.; Lewandowski, J. R. Unraveling the complexity of protein backbone dynamics with combined ^{13}C and ^{15}N solid-state NMR relaxation measurements. *Phys. Chem. Chem. Phys.* **2015**, *17*, 21997−22008.
(131) Donovan, K. J.; Jain, S. K.; Silvers, R.; Linse, S.; Griffin, R. G. Proton-Assisted Recoupling (PAR) in Peptides and Proteins. *J. Phys. Chem. B* **2017**, *121*, 10804−10817.
(132) De Paëpe, G.; Lewandowski, J. R.; Loquet, A.; Böckmann, A.; Griffin, R. G. Proton assisted recoupling and protein structure determination. *J. Chem. Phys.* **2008**, *129*, 245101.
(133) Mouyna, I.; Dellière, S.; Beauvais, A.; Gravelat, F.; Snarr, B.; Lehoux, M.; Zacharias, C.; Sun, Y.; de Jesus Carrion, S.; Pearlman, E.; Sheppard, D. C.; Latgé, J. P. What Are the Functions of Chitin Deacetylases in Aspergillus fumigatus? *Front. Cell. Infect. Microbiol.* **2020**, *10*, 28.
(134) Nishiyama, Y.; Frey, M. H.; Mukasa, S.; Utsumi, H. ^{13}C solid-state NMR chromatography by magic angle spinning ^{1}H T_1 relaxation ordered spectroscopy. *J. Magn. Reson.* **2010**, *202*, 135−139.

https://doi.org/10.1021/jacs.5c04054
J. Am. Chem. Soc. 2025, 147, 17416−17432